Polymerization-Induced Polymersome Fusion

Spyridon Varlas,[†] Robert Keogh,[†] Yujie Xie,[†,‡] Sarah L. Horswell,[†] Jeffrey C. Foster,*[†] and Rachel K. O'Reilly*[†]

[†]School of Chemistry, University of Birmingham, Edgbaston, Birmingham B15 2TT, United Kingdom
[‡]Department of Chemistry, University of Warwick, Gibbet Hill Road, Coventry CV4 7AL, United Kingdom

S *Supporting Information*

ABSTRACT: The dynamic interactions of membranes, particularly their fusion and fission, are critical for the transmission of chemical information between cells. Fusion is primarily driven by membrane tension built up through membrane deformation. For artificial polymersomes, fusion is commonly induced via the external application of a force field. Herein, fusion-promoted development of anisotropic tubular polymersomes (tubesomes) was achieved in the absence of an external force by exploiting the unique features of aqueous ring-opening metathesis polymerization-induced self-assembly (ROMPISA). The out-of-equilibrium tubesome morphology was found to arise spontaneously during polymerization, and the composition of each tubesome sample (purity and length distribution) could be manipulated simply by targeting different core-block degrees of polymerization (DPs). The evolution of tubesomes was shown to occur via fusion of "monomeric" spherical polymersomes, evidenced most notably by a step-growth-like relationship between the fraction of tubular to spherical nano-objects and the average number of fused particles per tubesome (analogous to monomer conversion and DP, respectively). Fusion was also confirmed by Förster resonance energy transfer (FRET) studies to show membrane blending and confocal microscopy imaging to show mixing of the polymersome lumens. We term this unique phenomenon polymerization-induced polymersome fusion, which operates via the buildup of membrane tension exerted by the growing polymer chains. Given the growing body of evidence demonstrating the importance of nanoparticle shape on biological activity, our methodology provides a facile route to reproducibly obtain samples containing mixtures of spherical and tubular polymersomes, or pure samples of tubesomes, of programmed length. Moreover, the capability to mix the interior aqueous compartments of polymersomes during polymerization-induced fusion also presents opportunities for its application in catalysis, small molecule trafficking, and drug delivery.
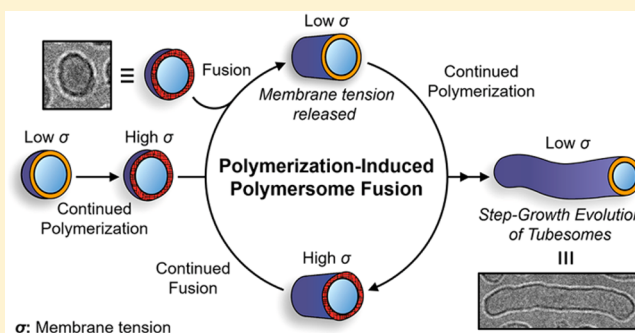
INTRODUCTION

The fusion of biological membranes is an essential process governing endo- and exocytosis, protein trafficking, fertilization, and viral infection in eukaryotic cells.[1−3] Proteins and other (macro)molecules are distributed throughout a cell, released into or internalized from the extracellular space via the action of membrane-bound vesicles.[4] Such vesicle-mediated transport occurs via the budding of new vesicular compartments from a cellular membrane and their downstream fusion with another membrane.[5] Vesicle budding and fusion processes do not transpire spontaneously, as lipid bilayer vesicles (liposomes) repel one another through electrostatic forces and possess membranes that are stabilized against deformation by a strong hydrophobic effect. Thus, the mechanisms of vesicle budding and fusion require an input of energy to occur. In biological systems, this energy is supplied by "**SNA**P **RE**ceptor", SNARE, proteins, which bring vesicles into close contact with the target surface and induce deformations in their membranes.[6−9] The tension built up through such elastic deformations is hypothesized to serve as the main driving force for vesicle fusion,[10] originating from an overall reduction in the tension-induced bending energy (E_b) of the system upon each fusion event.[11]

Although vesicle fusion is contingent on the action of proteins in biological systems, dissipative particle dynamics (DPD) simulations have shown that fusion between vesicles can occur spontaneously in the absence of proteins when two criteria are satisfied: (1) the particles can adhere to one another and maintain close contact and (2) there is sufficient membrane tension to overcome energetic barriers of fusion, of which the membrane bending energy dominates.[12] The bending energy of a membrane (E_b) is defined in eq 1

$$E_b = \sigma \Delta A + \oint \frac{k}{2} C^2 \, dA$$

(1)

where σ is the membrane tension, ΔA is the change in membrane surface area, k is the membrane bending rigidity, a

polymer specific property, and C is the local membrane curvature.[13,14] From this equation, it is clear that a buildup of tension within a vesicular membrane increases its bending energy, and the alleviation of this tension provides a significant driving force for vesicle fusion as it reduces the overall E_b of the system. Membrane tension is typically generated via the exertion of an external force. In biological systems, this force is applied by fusion proteins, although other mechanisms have also been discovered.[10]

Both experimental and DPD simulations have rigorously demonstrated the impact of membrane tension on the vesicular morphology and dynamics, showing that tension can be released by a number of pathways including vesicle hemifusion, fusion, membrane deformation, or membrane rupture.[12,15−18] For vesicles with σ sufficiently low that spontaneous membrane rupture occurs over prohibitively long time scales, fusion is the most probable pathway to release their membrane tension. Importantly, the mechanism of vesicle fusion appears to depend upon the nature of the membrane's amphiphilic constituents. Thus, fusion of liposomes occurs in a distinctly different manner compared to the fusion processes of amphiphilic block copolymer vesicles (also referred to as polymersomes) composed of either coil−coil or rod−coil blocks.[19−21] In the latter case, additional membrane tension is provided by the tendency of rod-like polymers to align, resisting the formation of nanostructures with high interfacial curvature. Indeed, DPD studies on fusion of rod−coil polymersome systems have shown that membrane tension scales with the length of the rod-like block.[18]

While the fusion mechanisms of liposomes and their application in biological systems have been studied extensively,[22−25] a very limited number of experimental studies have been carried out regarding the fusion of polymersomes.[26,27] This is due, in part, to the fact that polymersomes are most often prepared using conventional block copolymer self-assembly methodologies, such as solvent-switch or thin-film rehydration, operating under thermodynamically favorable conditions and thus their membranes are formed with low membrane tension, preventing their spontaneous fusion.[28−30] An alternative one-step route that allows for preparation of polymersomes at high concentrations is polymerization-induced self-assembly (PISA).[31−38] During PISA, amphiphilic block copolymer nano-objects are developed spontaneously upon chain-extension of a solvophilic steric stabilizer block using specific solvent-miscible monomers that gradually form solvophobic polymers as the length of the core-forming block increases, driving *in situ* self-assembly.[39−43] Based on the rate of polymerization propagation relative to self-assembly dynamics, kinetically trapped morphologies with high membrane tensions could theoretically be generated via PISA.[44]

Morphology diagrams have been constructed for PISA systems by varying externally controlled experimental parameters, such as the targeted degree of polymerization (DP) of the core-forming block, the overall solids concentration, or the core-block solubility, providing a roadmap to readily obtain pure polymersome nano-objects.[39,45,46] Typically, polymersomes occupy a narrow region of the phase space, requiring high solids concentrations and high DPs for their formation. In our recent report on aqueous ring-opening metathesis polymerization-induced self-assembly (ROMPISA), we observed that polymersomes occupied a uniquely broad region of the phase space over a wide range of core-forming monomers and targeted DPs.[47] This phenomenon was mainly attributed

to the influence of the rigid rod-like nature of polynorbornenes on their packing within the assembled nanostructures, disfavoring higher interfacial curvature structures, such as spherical or worm-like micelles. In addition to the unique morphology evolution observed for nano-objects prepared by ROMPISA,[47] it was also apparent that the developed polymersomes were of similar size and shape over a broad range of targeted core block DPs. This result was in stark contrast to polymersomes obtained via PISA mediated by reversible addition−fragmentation chain transfer (RAFT) polymerization, which generally increase in size or evolve toward more complex morphologies, such as multicomponent vesicles or lamellae, as the core block DP is further increased.[48−51] Since it did not appear that polymersomes prepared via ROMPISA could minimize their bending energies through membrane rearrangement processes (no observable changes in ΔA or C), we wondered whether the nano-object membranes were becoming "charged" with high tension during polymerization as the length of their constituent polymers increased to compensate for their static curvature and surface area. Thus, we envisioned that ROMPISA may represent an ideal platform for studying the fusion behavior of polymersomes formed from rod-like polymers.

As discussed above, good intervesicle adhesion and increased membrane tension must both be present to allow for membrane fusion events to occur. Our previous studies on aqueous ROMPISA were carried out using a polyamine corona-forming block, which, under the experimental conditions utilized, produced nano-objects with positive surface charge.[47,52] As a result, no evidence of polymersome adhesion and fusion was observed in these systems, as these processes were effectively prohibited by strong interparticle repulsion. We therefore hypothesized that the structure of the hydrophilic stabilizer block could be tuned to modulate the fusion behavior of ROMPISA polymersomes, inducing the evolution of large and/or non-spherical bilayer structures.

Herein, we evaluate this hypothesis by investigating the influence of macroinitiator chemistry, reaction conditions, and targeted core block DP upon the morphology of diblock copolymer nano-objects prepared via aqueous dispersion ROMPISA. In particular, it was found that the absence of charges on the outer surface of the developed nano-objects facilitated polymerization-induced polymersome fusion and *in situ* evolution of an increasing population of progressively longer tubular polymersomes—tubesomes—upon increasing targeted DP of the core-forming block. Polymerization kinetic monitoring and exhaustive nano-object characterization revealed that the onset of polymersome fusion occurred at a critical core block DP followed by an acceleration in rate of tubesome growth. Importantly, the development of kinetically favorable tubesomes via polymerization-induced fusion of spherical polymersome building blocks was found to precisely follow a step-growth-like motif, where a larger number of fusion events per particle was noticed for samples with larger tubesome fractions. Overall, our study provides insight into the fusion mechanisms of artificial polymeric vesicles and access to facile one-pot preparation of anisotropic tubular polymersomes via aqueous ROMPISA, establishing them as an attractive alternative nanoplatform for numerous biomedical applications owing to their well-documented superior physicochemical properties compared to their spherical counterparts.[53−57]

■ RESULTS

ROMP-mediated PISA in aqueous environment requires solubilization of the utilized metathesis catalyst through modification of one or more of its surrounding ligands with hydrophilic moieties.[52,58,59] While several strategies have been developed thus far to generate water-soluble Ru-based metathesis catalysts, often through transformations involving either N-heterocyclic carbene (NHC) or pyridine ligands,[60,61] such catalysts typically suffer from reduced activity compared to the unmodified precursor in organic solvent.[62] In this study, rapid polymerization kinetics were desired to obtain kinetically trapped morphologies during ROMPISA; thus, our previously reported open-to-air two-step ROMPISA procedure was adopted, involving the synthesis of a hydrophilic macroinitiator via ROMP in organic media prior to PISA, which affords fast and controllable polymerization in aqueous media, as shown in Scheme 1.[52]

Scheme 1. Schematic Representation of the Synthetic Route Followed for the Development of P(NB-R)$_{11}$-b-P(NB-MEG)$_n$ Diblock Copolymer Nano-Objects via Aqueous Dispersion ROMPISA, Using Either a Water-Soluble P(NB-Amine)$_{11}$ or P(NB-PEG)$_{11}$ Macroinitiator
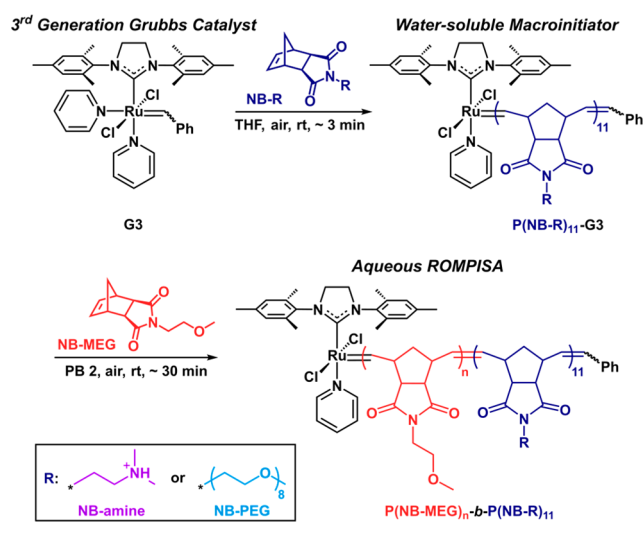
To perform aqueous ROMPISA using a macroinitiator approach, a water-soluble polymer was first prepared by polymerizing a hydrophilic monomer, in this case either a tertiary amine functional norbornene (**NB-amine**) or a PEGylated norbornene (**NB-PEG**), via ROMP in a water-miscible solvent (i.e., THF) using the commercially available third-generation Grubbs catalyst (**G3**). The resulting macroinitiator was subsequently chain-extended upon dilution with an acidic aqueous solution of the core-forming monomer (**NB-MEG**), resulting in the *in situ* formation of amphiphilic diblock copolymer nano-objects under dispersion polymerization conditions. The presence of acid is of vital importance for controlled aqueous ROMP using **G3**, as it promotes pyridine ligand dissociation to generate the active catalyst species and limits catalyst deactivation by OH$^-$ species.[52,60,63]

Previously, we demonstrated that typical PISA morphologies (i.e., spherical micelles, worm-like micelles, and vesicles) could be readily accessed using this macroinitiator approach and that uniquely small, spherical polymersomes were obtained over a broad range of compositions for P(NB-amine)$_{12}$-b-P(NB-X)$_n$

diblock copolymers with $60 \leq n \leq 180$.[47] In this study, our efforts initially focused on further extending the core block DP beyond 180 to determine whether the system would evolve beyond vesicles toward other higher-order morphologies. We hypothesized that the cationic amine corona would provide an additional barrier against morphological transitions beyond spherical polymersomes due to electrostatic repulsive forces between particles, effectively limiting fusion events and other interparticle assembly pathways.[64] Toward this end, a series of ROMPISA reactions were carried out using a P(NB-amine)$_{11}$ macroinitiator ($M_{n,NMR}$ = 2.5 kDa, $M_{n,SEC}$ = 2.6 kDa, $Đ_M$ = 1.22, Figures S7−S9, and Table S2) targeting DPs of 120, 180, 240, 300, and 420 for the core-forming P(NB-MEG) block by varying the initial [NB-MEG]/[G3] feed ratio. All polymerizations were performed in acidic phosphate buffer (pH 2, PB2) at a total solids concentration of 1 wt % in the presence of 10% v/v THF. Following ROMPISA, P(NB-amine)$_{11}$-b-P(NB-MEG)$_n$ diblock copolymers were analyzed by ^{1}H-NMR spectroscopy for monomer conversion calculation, and size-exclusion chromatography (SEC) to determine number-average molecular weight (M_n) and dispersity ($Đ_M$) values, while the resulting nano-objects were characterized by dynamic light scattering (DLS), zeta potential analysis, and transmission electron microscopy (TEM) imaging. A summary of the obtained results is provided in Figure 1 and in the Supporting Information (Figures S10 and S14−S17 and Tables S3 and S5).

In particular, controlled polymerizations were achieved in all cases, with quantitative monomer conversions (>99%) achieved after ∼30 min of polymerization time yielding P(NB-amine)$_{11}$-b-P(NB-MEG)$_n$ diblock copolymers with narrow and symmetrical molecular weight distributions, low dispersity values ($Đ_M \leq 1.14$), and $M_{n,SEC}$ that increased linearly with the initial feed ratio of monomer to catalyst (Figure 1A,B and Table S3). Consistent with our previous report, a uniform population of spherical polymersomes with D_h = 47.8 ± 1.7 nm was obtained when targeting DP$_{P(NB-MEG)}$ = 180, as judged by DLS analysis and TEM imaging. As the targeted core block DP was further increased to 240 and 300, only a slight increase in the average hydrodynamic diameter of the polymersomes to 59.9 ± 0.3 and 61.4 ± 1.2 nm, respectively, was observed, whereas at DP$_{P(NB-MEG)}$ = 420, ill-defined non-spherical nano-objects with D_h = 83.2 ± 0.9 nm were developed. In all cases, zeta potential analysis confirmed the presence of positive charges on the outer surface of the obtained nano-objects and their cationic character under ROMPISA-mimicking conditions (zeta potential > + 21 mV, at pH 2.0; Figures 1C,D,F, S14, and S17 and Table S5).

To gain further insight into the self-assembly process, dry-state TEM images were analyzed using image processing software to calculate average particle length (L_{ave}, the distance in nm along the longest nano-object axis), average maximum dimension (S_{ave}, diameter for spherical polymersomes or length for non-spherical ones) and average circularity values (C_{ave}) for each formulation. A full description of the image analysis methodology applied herein is provided in the Supporting Information. As shown in Figures 1F, S15 and S16, S_{ave} values increased concurrently with D_h, although these values were systematically lower than the diameters measured by DLS likely due to particle shrinkage upon drying. In addition, the nano-object C_{ave} values—a ratio of the particle's area to its perimeter—remained relatively constant, ranging between 0.65 and 0.8 across the series with the exception of
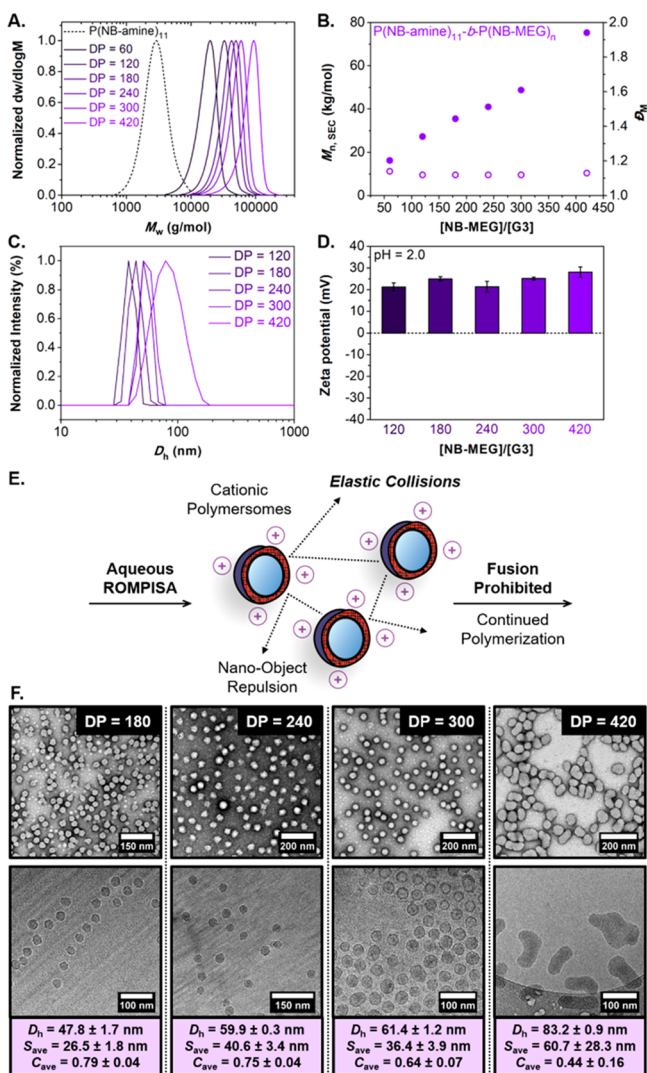
Figure 1. Characterization summary for the series of $P(NB\text{-}amine)_{11}\text{-}b\text{-}P(NB\text{-}MEG)_n$ diblock copolymer nano-objects. (A) Normalized SEC RI molecular weight distributions, and (B) evolution of M_n (filled circles) and $Đ_M$ (empty circles) values with increasing targeted $DP_{P(NB\text{-}MEG)}$ calculated from SEC analysis for $P(NB\text{-}amine)_{11}\text{-}b\text{-}P(NB\text{-}MEG)_n$ diblock copolymers prepared via aqueous ROMPISA. $M_{n,\ SEC}$ and $Đ_M$ values were calculated from PS standards using THF + 2% v/v NEt_3 as the eluent. (C) Normalized intensity-weighted size distributions obtained by DLS for $P(NB\text{-}amine)_{11}\text{-}b\text{-}P(NB\text{-}MEG)_n$ diblock copolymer nano-objects. (D) Zeta potential values for $P(NB\text{-}amine)_{11}\text{-}b\text{-}P(NB\text{-}MEG)_n$ diblock copolymer nano-objects measured from microelectrophoretic analysis in PB2. (E) Schematic representation of interpolymersome repulsion restricting fusion events and further morphological evolution. (F) Representative dry-state (top row) and cryo-TEM (bottom row) images of $P(NB\text{-}amine)_{11}\text{-}b\text{-}P(NB\text{-}MEG)_n$ diblock copolymer nano-objects, and summary of D_h values determined from DLS, and S_{ave} and C_{ave} values calculated from image analysis of the dry-state TEM images. Dry-state samples were stained using 1 wt % uranyl acetate (UA) solution.

the $P(NB\text{-}amine)_{11}\text{-}b\text{-}P(NB\text{-}MEG)_{420}$ nanostructures. A dramatic decrease in C_{ave} to 0.44 ± 0.16 was measured for this sample, where the predominant morphology appeared to be of non-spherical shape. Taken together, these data support our hypothesis that electrostatic repulsive forces originating from cationic charges within the particle coronae resist morpho-

logical evolution via pathways involving interactions between multiple nano-objects (i.e., fusion; Figure 1E).

To promote fusion, it was apparent that surface charge should be minimized to facilitate adhesive collisions between nano-objects. We envisioned that, by changing the chemistry of the stabilizer block pendant groups from cationic tertiary amines to non-ionic poly(ethylene glycol) (PEG, $M_n \approx 350$ g mol^{-1}) units, the energy barrier of polymersome fusion would be reduced, rendering fusion the operative pathway of morphological evolution. To this extent, a series of $P(NB\text{-}PEG)_{11}\text{-}b\text{-}P(NB\text{-}MEG)_n$ diblock copolymer nano-objects were prepared using the same two-step ROMPISA methodology as previously discussed, this time employing **NB-PEG** as the corona-forming monomer to prepare a water-soluble $P(NB\text{-}PEG)_{11}$ macroinitiator ($M_{n,NMR} = 5.5$ kDa, $M_{n,SEC} = 5.3$ kDa, $Đ_M = 1.20$, Figures S25−S27 and Table S8). As before, aqueous ROMPISA reactions using **NB-MEG** as the core-forming monomer were conducted at [solids] = 1 wt % in 90:10 PB2/THF. Core-block DPs of 40, 60, 120, 140, 180, 240, 260, and 300 were targeted to accurately monitor the evolution of particle morphology as a function of copolymer composition.

Similar to the **P(NB-amine)**-based formulations, ^{1}H-NMR spectroscopic analysis showed complete monomer conversions (>99%) after ~30 min, and SEC analysis of the resulting $P(NB\text{-}PEG)_{11}\text{-}b\text{-}P(NB\text{-}MEG)_n$ diblock copolymers confirmed excellent polymerization control across the series ($Đ_M \leq 1.16$; Figures 2A,B and S28 and Table S9). In addition, TEM imaging and DLS analysis revealed the formation of small spherical polymersomes with D_h values of 25.9 ± 1.9 nm, 34.9 ± 3.6 nm and 47.5 ± 1.1 nm when targeting $DP_{P(NB\text{-}MEG)} = 40$, 60 and 120, respectively (Figures 2C,F and S35−S38 and Table S11). It is supposed that the membrane thickness of the polymersomes rapidly increases inward upon targeting higher core-block DPs, reducing the volume of their inner aqueous compartments, analogous to a previous study on polymersomes developed via RAFT-mediated PISA.[33] Due to the uniquely small size of the polymersomes prepared herein, it was sometimes difficult to identify the presence of their inner lumen and accurately determine their membrane thickness from the acquired TEM images. To further prove the polymersome morphology, static light scattering (SLS) analysis was carried out on the spherical polymersome samples with $DP_{P(NB\text{-}MEG)} = 40$ and 60. In particular, measured R_g/R_h values were 0.87 and 0.82, respectively, with calculated N_{agg} values of 439 and 827 (Figures S32 and S33 and Table S12). Based on the fact that the measured R_g/R_h values are intermediate between what would be typically expected for hollow spherical polymersomes ($R_g/R_h = 1.0$) and spherical core−shell micelles ($R_g/R_h \approx 0.78$), as well as the markedly high N_{agg} values compared to expected values for spherical micelles,[85] these results support our hypothesis of hollow nanostructures with rather small inner compartments. Moreover, the observed decrease in R_g/R_h ratio with increasing $DP_{P(NB\text{-}MEG)}$ is consistent with our proposal of assemblies of similar hydrodynamic volume but progressively increasing membrane thickness, and as a consequence reduced inner lumen volume.

In stark contrast to the **P(NB-amine)**-based series, significant nano-object elongation was clearly evident when the targeted core-block DP was increased above 120, based on observations from acquired dry-state and cryo-TEM images. In fact, for the $P(NB\text{-}PEG)_{11}\text{-}b\text{-}P(NB\text{-}MEG)_n$ samples where n = 140, 180, 240, and 260, tubular polymersomes (so-called

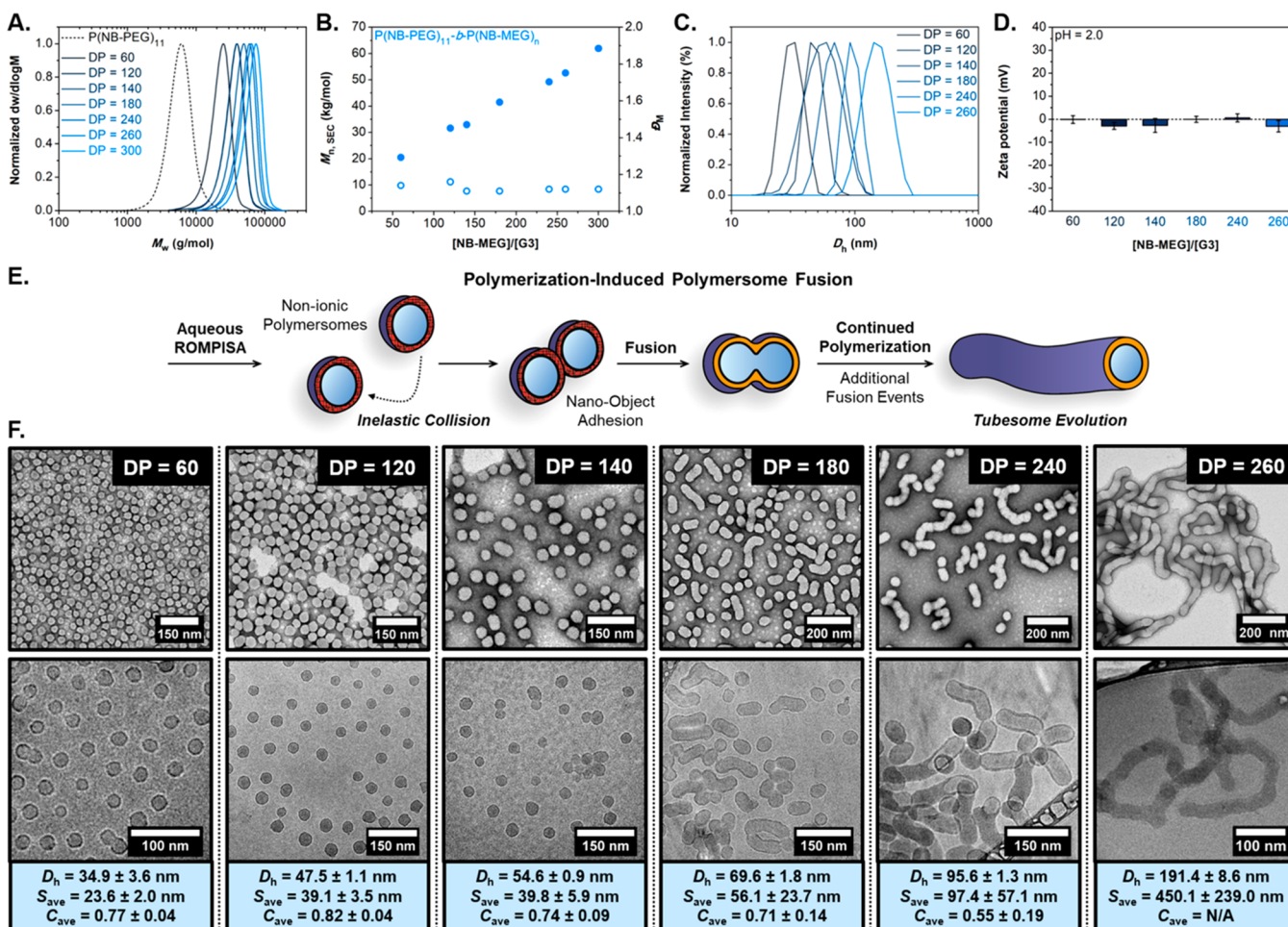**Figure 2.** Characterization summary for the series of $P(NB\text{-}PEG)_{11}\text{-}b\text{-}P(NB\text{-}MEG)_n$ diblock copolymer nano-objects. (A) Normalized SEC RI molecular weight distributions, and (B) evolution of M_n (filled circles) and $Đ_M$ (empty circles) values with increasing targeted $DP_{P(NB\text{-}MEG)}$ calculated from SEC analysis for $P(NB\text{-}PEG)_{11}\text{-}b\text{-}P(NB\text{-}MEG)_n$ diblock copolymers prepared via aqueous ROMPISA. $M_{n,\,SEC}$ and $Đ_M$ values were calculated from PS standards using THF + 2% v/v NEt₃ as the eluent. (C) Normalized intensity-weighted size distributions obtained by DLS for $P(NB\text{-}PEG)_{11}\text{-}b\text{-}P(NB\text{-}MEG)_n$ diblock copolymer nano-objects. (D) Zeta potential values for $P(NB\text{-}PEG)_{11}\text{-}b\text{-}P(NB\text{-}MEG)_n$ diblock copolymer nano-objects measured from microelectrophoretic analysis in PB2. (E) Schematic representation of tubesome evolution via polymerization-induced polymersome fusion. (F) Representative dry-state (top row) and cryo-TEM (bottom row) images of $P(NB\text{-}PEG)_{11}\text{-}b\text{-}P(NB\text{-}MEG)_n$ diblock copolymer nano-objects, and summary of D_h values determined from DLS, and S_{ave} and C_{ave} values calculated from image analysis of the dry-state TEM images. Dry-state samples were stained using 1 wt % uranyl acetate (UA) solution.

"tubesomes") of increasing length were obtained, as evidenced by both DLS and TEM image analyses (Figures 2C,F and S35−S38 and Table S11). Typically, cryo-TEM serves as the main imaging tool for observation of non-spherical polymersomes, as morphological discrepancies of nano-objects can occur during the drying process. However, in our case the morphology of tubular nanostructures could be effectively retained under dry-state TEM conditions, owing to the high glass transition temperature (T_g) values of polynorbornene-based polymers (T_g of $P(NB\text{-}MEG)_{180}$ homopolymer = 118.2 °C, Figure S6).

From dry-state TEM image processing, the calculated S_{ave} values also increased with increasing targeted $DP_{P(NB\text{-}MEG)}$, while C_{ave} values decreased consistently across the series (note that circularity could not be accurately calculated for the $P(NB\text{-}PEG)_{11}\text{-}b\text{-}P(NB\text{-}MEG)_{260}$ sample due to the lack of a sufficient number of "well-isolated" particles in the TEM images). It was also apparent that the populations of spherical and tubular polymersomes became increasingly biased toward the latter upon gradually increasing the targeted core block DP.

Indeed, a nearly pure morphology of highly anisotropic tubesomes was present in the $P(NB\text{-}PEG)_{11}\text{-}b\text{-}P(NB\text{-}MEG)_{260}$ sample. In this case, cryo-TEM imaging was challenging to perform as the tubesomes were located in relatively thick vitrified ice layers owing to their large size and irregular shape.[57] It should also be noted that the average width of formed tubesomes did not appear to significantly vary beyond the critical $DP_{P(NB\text{-}MEG)} = 140$ sample, whereas a further increase of the core-forming block beyond DP = 260 resulted in macroscopic precipitation due to instability of the developed nano-objects, most likely owing to their exceedingly increased length and hydrophobicity. Contrary to the zeta potential values measured for $P(NB\text{-}amine)_{11}\text{-}b\text{-}P(NB\text{-}MEG)_n$ nano-objects, the presence of non-ionic PEG chains on the outer layer of both the $P(NB\text{-}PEG)_{11}\text{-}b\text{-}P(NB\text{-}MEG)_n$ spherical and tubular polymersomes was readily reflected on the findings from microelectrophoretic analysis, as zeta potential values of approximately 0 mV were measured in all cases (Figure 2D and Table S11). These results support the idea that reduced interparticle repulsion, affected by changes in

corona chemistry and particle surface charge, led to notable polymersome fusion during ROMPISA, implying that morphological evolution was now occurring by a different pathway than that observed in the case of the **P(NB-amine)**-based system (Figure 2E).

As a final illustration of the importance of particle corona chemistry on the self-assembly behavior, the ROMPISA reactions for preparation of **P(NB-amine)$_{11}$**-*b*-**P(NB-MEG)$_n$** nano-objects were repeated in the presence of a high concentration of NaCl in PB2 (i.e., [NaCl] = 100 mM). We supposed that the presence of salt would act to partially screen the positive charge in the nano-object coronae, facilitating the occurrence of productive inelastic collisions and thus increasing the incidence of fusion events. Full characterization of the synthesized diblock copolymers and the resulting nanostructures is provided in detail in the Supporting Information (Figures S20−S24 and Tables S6 and S7). In brief, polymerization control was not affected by the presence of NaCl in the reaction medium; however, particle fusion was observed between polymersomes with **P(NB-amine)** coronae in this case, with the onset of fusion shifted toward higher core-block DP relative to the **P(NB-PEG)**-based series. Indeed, nearly pure morphologies of long, tubular polymersomes could be obtained for the **P(NB-amine)** system in the presence of NaCl, highlighting the importance of the role of corona chemistry in determining the assembly pathway during ROMPISA.

While marked differences in corona charge between the **P(NB-amine)**- and **P(NB-PEG)**-based samples represented a probable explanation for the noticeable variation in the assemblies developed for each series, we also considered that the unique tubesome morphology could potentially arise from differences in ROMPISA kinetics between the two series. To compare the relative rates of both polymerization and morphological evolution processes, kinetic monitoring experiments were performed using complementary characterization techniques. Aqueous ROMPISA reactions targeting either **P(NB-amine)$_{11}$**-*b*-**P(NB-MEG)$_{300}$** or **P(NB-PEG)$_{11}$**-*b*-**P(NB-MEG)$_{260}$**−polymers with approximately the same M_n and $Đ_M$ values−were sampled at various time intervals over a period of 30 min, and the sample aliquots were quenched via the addition of ethyl vinyl ether (EVE) for deactivation of the Ru-based catalyst (Figures S11 and S29). In both cases, these samples were then analyzed by ^{1}H-NMR spectroscopic and SEC analyses to determine polymerization conversion and "livingness", while DLS analysis of samples diluted immediately after quenching was used to monitor changes in nano-object size as polymerization progressed. It should be mentioned that dry-state TEM imaging of the quenched samples was also attempted, although significant discrepancies were observed in the TEM images compared with those shown in Figures 1 and 2, attributed to the presence of plasticizing EVE molecules incorporated within the polymersome membranes leading to equilibration of the samples toward more thermodynamically favored products upon drying on the TEM grids (Figure S41). However, dry-state TEM imaging of samples taken after completion of each kinetic run without addition of EVE agreed well with our previous findings for aqueous ROMISA reactions targeting DP$_{P(NB-MEG)}$ = 300 or 260, respectively.

Based on the original plots of monomer conversion vs time (Figures S12 and S30), it was found in both cases that the onset of nano-object micellization occurred at a very early stage of the polymerization (i.e., at *ca.* 0.3 min and 35% **NB-MEG** conversion), before which the rate of polymerization in solution appeared to be faster compared to polymerization within the nano-object cores.[66,67] Thus, we considered monomer conversion after this nucleation point in our subsequent analysis. As shown in Figure 3A, both polymer-
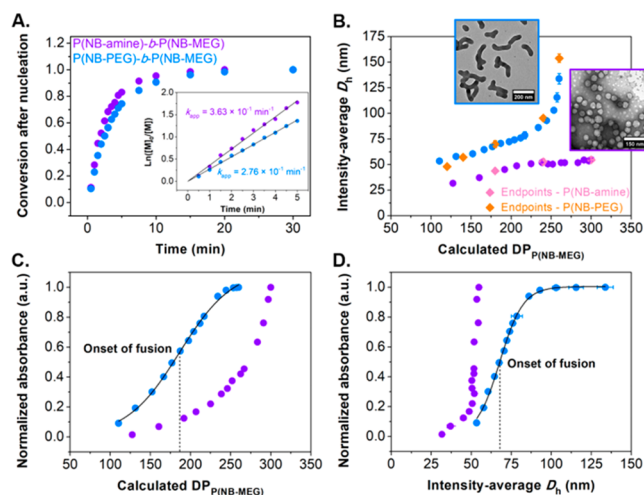

Figure 3. Summary of aqueous ROMPISA kinetic monitoring experiments. (A) Monomer conversion after particle nucleation vs polymerization time kinetic plots for synthesis of **P(NB-amine)$_{11}$**-*b*-**P(NB-MEG)$_{300}$** (purple circles) and **P(NB-PEG)$_{11}$**-*b*-**P(NB-MEG)$_{260}$** (blue circles) diblock copolymers via aqueous ROMPISA, as determined by ^{1}H-NMR spectroscopy in DMSO-d_6 with 1,3,5-trioxane as an external standard. The inset shows the corresponding semilogarithmic plots for the determination of pseudo-first-order kinetic constants (k_{app}). (B) Evolution of intensity-average D_h, as determined by DLS analysis of aliquots for the same **P(NB-amine)$_{11}$**-*b*-**P(NB-MEG)$_{300}$** (purple circles) and **P(NB-PEG)$_{11}$**-*b*-**P(NB-MEG)$_{260}$** (blue circles) diblock copolymer nano-objects withdrawn during kinetic monitoring, as a function of DP$_{P(NB-MEG)}$ calculated from conversion. The insets show representative dry-state TEM images of samples obtained after completion of each ROMPISA process without EVE addition. The pink and orange diamonds represent D_h values determined from the end-point measurements shown in Figures 1 and 2 for the **P(NB-amine)**- and **P(NB-PEG)**-based samples, respectively. (C) Normalized absorbance, as determined by *in situ* turbidimetric analysis during each polymerization for synthesis of **P(NB-amine)$_{11}$**-*b*-**P(NB-MEG)$_{300}$** (purple circles) and **P(NB-PEG)$_{11}$**-*b*-**P(NB-MEG)$_{260}$** (blue circles) diblock copolymer nano-objects, as a function of DP$_{P(NB-MEG)}$ calculated from conversion. The black line corresponds to a standard sigmoidal logistic fit, showing an inflection point at DP$_{P(NB-MEG)}$ ≈ 185 highlighted by the dashed line that corresponds to the onset of polymersome fusion (R^2 = 0.998). (D) Normalized absorbance, as determined by *in situ* turbidimetric analysis during each polymerization for synthesis of **P(NB-amine)$_{11}$**-*b*-**P(NB-MEG)$_{300}$** (purple circles) and **P(NB-PEG)$_{11}$**-*b*-**P(NB-MEG)$_{260}$** (blue circles) diblock copolymer nano-objects, vs intensity-average D_h measured from DLS analysis. The black line corresponds to a standard sigmoidal logistic fit, with an inflection point at D_h ≈ 68 nm highlighted by the dashed line that corresponds to the onset of polymersome fusion (R^2 = 0.998).

ization processes exhibited pseudo-first order kinetics after the point of nucleation, as judged by the semilogarithmic plots, with quantitative conversions (>99%) achieved after 30 min. Importantly, propagation rates for both samples were found not to vary significantly ($t_{1/2}$ = 1.9 and 2.5 min were calculated for **P(NB-amine)**- and **P(NB-PEG)**-based formulations, respectively). Thus, we were able to rule out differential

polymerization kinetics as an explanation for the distinct differences in fusion behavior between the two nano-object series. Moreover, SEC analysis of selected samples obtained from kinetic monitoring experiments revealed the linear evolution of $M_{n,\,SEC}$ values with increasing **NB-MEG** conversion and verified the living character of both ROMPISA processes (Figures S13 and S31 and Tables S4 and S10).

In contrast to the ^{1}H-NMR spectroscopic analysis, a significant difference was observed in the slopes of the plots showing the time-dependent evolution of intensity-average D_h values, as measured by DLS (Figures S18A and S39A). To further emphasize this difference, the average diameter values corresponding to the developed diblock copolymer nano-objects at each time point were correlated to the core block DP calculated from conversion (Figure 3B). For the **P(NB-amine)**-based samples, it was evident that intensity-average D_h values increased linearly up to *ca.* $DP_{P(NB-MEG)} = 210$, after which the measured diameter remained constant independent of the DP of the growing **P(NB-MEG)** block. By comparison, a similar linear D_h increase was observed early in the polymerization of the **P(NB-PEG)**-based system; however, above a similar $DP_{P(NB-MEG)}$ threshold, the average nano-object diameter increased exponentially with increasing polymer DP. These data are consistent with the observations made by TEM imaging (Figures 1 and 2), where the **P(NB-PEG)$_{11}$-*b*-P(NB-MEG)$_n$** nanostructure composition approached a pure morphology of long, tubular polymersomes as the DP of core-forming **P(NB-MEG)** was increased from 180 to 260, while **P(NB-amine)$_{11}$-*b*-P(NB-MEG)$_n$** diblock copolymers only yielded small spherical polymersomes with minor size differences as the targeted core block DP varied between 180 and 300.

As a final method for direct kinetic comparison, both ROMPISA procedures were monitored via *in situ* turbidimetric analysis using UV−vis spectroscopy. Variations in transmitted light (% transmittance) at $\lambda = 550$ nm were measured over the course of the reactions, and the observed reduction in % transmittance (or increase in absorbance) was assumed to arise from increased scattering of the incident light by the growing particles in solution (Figures S18B and S39B). For Rayleigh scattering, relevant for particles smaller than the wavelength of the incident light, the scattering intensity can be correlated to the diameter of the scattering species through a power law relationship.[68] Thus, the decrease in transmitted light intensity can be viewed in the lens of increasing particle size. Upon comparing the data obtained from turbidimetric analysis to those obtained from ^{1}H-NMR spectroscopy and DLS analysis, a few key relationships evidently emerged. Figure 3C shows the change in absorbance (related in this case to scattering intensity) as a function of the core block DP calculated from conversion. For the **P(NB-amine)**-based sample, the curve scaled according to a power law relationship, consistent with increased scattering by particles of progressively increasing size. In contrast, a sigmoidal relationship was noticed for the **P(NB-PEG)**-based sample, with an initial slope of power-law scaling and an inflection at $DP_{P(NB-MEG)} \approx 185$. The DP value at this inflection point is of great significance, as it corresponds to the critical DP at which the onset of polymersome fusion was also observed in previous end-point experiments (Figure 2). This result can be rationalized as follows: (1) spherical polymersomes initially increase in diameter, leading to increased scattering according to the expected power law relationship, (2) above a certain DP threshold, fusion of

spherical polymersome building blocks begins favoring the development of tubesomes, and (3) the rate of change in the size of the particles increases dramatically, but is also accompanied by a proportional decrease in the overall number of particles, with the net effect being a decreased dependence of the scattered light intensity on the polymer DP. The same trends were observed when comparing the intensity-average D_h of the prepared diblock copolymer nano-objects, as measured by DLS analysis, to their corresponding absorbance values (Figure 3D), with an inflection point being evident for the **P(NB-PEG)$_{11}$-*b*-P(NB-MEG)$_n$** sample at $D_h \approx 68$ nm corresponding to a $DP_{P(NB-MEG)}$ of approximately 180 and to the time at which the onset of polymersome fusion occurs.

The above experiments provide indirect evidence of polymerization-induced polymersome fusion based on the exponential size increase of the tubesomes with increasing DP of the core-forming block and the presence of apparent intermediate fusion stages in the obtained TEM images (Figure S40). To directly verify and monitor polymersome fusion, a series of Förster resonance energy transfer (FRET) experiments were carried out, which involve the non-radiative transfer of absorbed energy from a donor to an acceptor fluorophore. The excited acceptor then emits a photon, with the net effect being that excitation of the donor fluorophore results in fluorescence emission of the acceptor. Importantly, the FRET process requires the two species to be in close contact for the energy transfer to occur (i.e., distances ≤10 nm). Thus, FRET provides a distance-dependent measurement of the dynamic activity of the two fluorescent compounds on the nanoscale.[69]

To evaluate polymersome membrane fusion using FRET in our **P(NB-PEG)-*b*-P(NB-MEG)** system, donor and acceptor fluorophores, that form a FRET pair when in close proximity, were incorporated into the developed polymer nanostructures. In particular, aminochloromaleimide (ACM) was chosen as the donor molecule based on its synthetic simplicity, small size, and high quantum yield in non-polar environments.[70] To provide good spectral overlap, Rhodamine B (RhB) was employed as the acceptor fluorophore (Figure 4B). Both species were introduced via coupling to norbornene moieties for the synthesis of **NB-ACM** and **NB-RhB** monomers, respectively, such that they could be directly polymerized and would remain covalently linked to the prepared copolymers during ROMPISA, avoiding a false indication of FRET behavior arising from diffusion of free fluorophore molecules between nano-objects. Our previously described aqueous ROMPISA procedure was then appropriately modified to introduce a short run of each fluorescent monomer as an intermediate block between the corona- and core-forming segments. In brief, **NB-PEG** was first polymerized via solution ROMP in THF using **G3** for synthesis of a **P(NB-PEG)$_{11}$** macroinitiator. Then, a solution of either **NB-ACM** or **NB-RhB** monomer in THF was added to the macroinitiator solution for synthesis of the second fluorophore-containing block (Figures S44 and S45 and Table S13). In the final step, each diblock copolymer macroinitiator was chain-extended using an acidic aqueous solution of **NB-MEG**, resulting in development of **P(NB-PEG)$_{11}$-*b*-P(NB-ACM)$_m$-*b*-P(NB-MEG)$_n$** and **P(NB-PEG)$_{11}$-*b*-P(NB-RhB)$_{m/2}$-*b*-P(NB-MEG)$_n$** triblock copolymer nano-objects via ROMPISA (**NB-ACM/NB-RhB** molar ratio = 2:1; Figure 4A-I).

As shown in Figure 4A-II, we hypothesized that FRET would arise between ACM- and RhB-functionalized particles
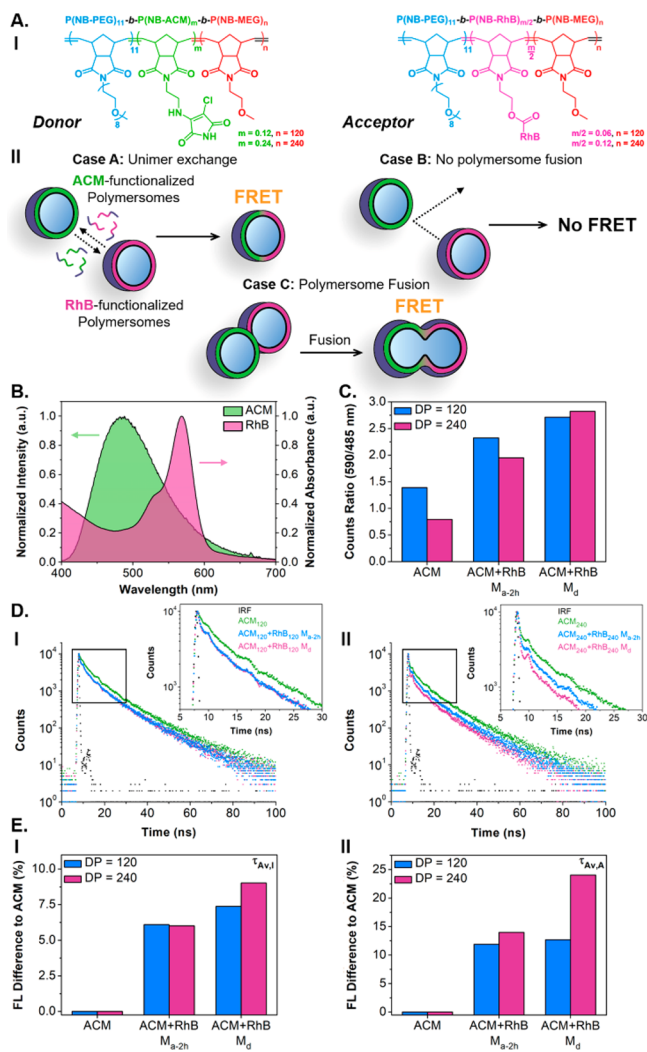
Figure 4. Summary of FRET results for pure **P(NB-PEG)$_{11}$-b-P(NB-ACM)$_m$-b-P(NB-MEG)$_n$** triblock copolymer nano-objects (ACM$_n$), and resulting ACM$_n$+RhB$_n$ M$_{a-2h}$ and ACM$_n$+RhB$_n$ M$_d$ samples (n = 120 and 240) for direct monitoring of polymersome membrane fusion. (A) Structures of **P(NB-PEG)$_{11}$-b-P(NB-ACM)$_m$-b-P(NB-MEG)$_n$** (donor) and **P(NB-PEG)$_{11}$-b-P(NB-RhB)$_{m/2}$-b-P(NB-MEG)$_n$** (acceptor) triblock copolymers prepared via aqueous ROMPISA (I), and schematic representation of potential outcomes from polymersome mixing experiments (II). (B) Spectral overlap between ACM fluorescence emission and RhB absorption spectra. For ACM$_n$, ACM$_n$+RhB$_n$ M$_{a-2h}$ and ACM$_n$+RhB$_n$ M$_d$ samples: (C) Counts ratio of the donor ($\lambda_{em.\ ACM}$ = 485 nm) and acceptor ($\lambda_{em.\ RhB}$ = 590 nm) fluorescence emission peaks. (D) Fluorescence lifetime decay profiles of (I) n = 120 and (II) n = 240 samples. (E) Comparison of average fluorescence lifetime values, expressed as % difference relative to the pure ACM$_n$ nano-objects, obtained using (I) $\tau_{Av,I}$ and (II) $\tau_{Av,A}$ fitting models.

only when (1) unimer exchange between particles was occurring on the time scale of the experiment; or (2) fusion between spherical polymersomes occurred, creating regions of close fluorophore contact within the fused tubular polymersome membranes. In the absence of both, no FRET would be expected. Since we were operating under the assumption that fusion events only occurred during polymerization, it was important to compare samples containing each fluorophore that were mixed during ROMPISA prior to the point at which full monomer conversion was reached, to those mixed after

completion of the polymerization in order to confirm this hypothesis.

Thus, two sets of ROMPISA reactions targeting **P(NB-MEG)** DPs of 120 (below fusion threshold) and 240 (above fusion threshold) were carried out using either **P(NB-PEG)$_{11}$-b-P(NB-ACM)$_m$** or **P(NB-PEG)$_{11}$-b-P(NB-RhB)$_{m/2}$** diblock copolymer macroinitiator under otherwise identical polymerization conditions. Equal amounts of pure ACM- and RhB-containing samples were then mixed after 1 min of polymerization time ($ca. \sim$ 50% **NB-MEG** conversion), at which point initial particle nucleation had occurred but polymerization was still incomplete. These samples, mixed during polymerization (M$_d$), were compared against the corresponding ones in which the ACM- and RhB-functionalized triblock copolymer nano-objects were mixed after polymerization for either 2h (M$_{a-2h}$) or 24h (M$_{a-24h}$). In the latter case, no fusion was expected to occur for either sample due to the lack of a driving force. Detailed characterization of resulting triblock copolymers and nano-objects is provided in the Supporting Information (Figures S46–S51 and Tables S14–S16).

In summary, successful attachment of the fluorophore molecules on the formed polymers was confirmed by performing SEC analysis of the diblock macroinitiators with UV detection at λ_{ACM} = 360 nm or λ_{RhB} = 545 nm where complete overlap between the RI and UV traces was observed. Importantly, DLS analysis and dry-state TEM imaging of the pure ACM- and RhB-functionalized samples, as well as the M$_{a-24h}$ and M$_d$ mixed samples, showed that the triblock copolymer architecture did not affect the self-assembly process of the resulting nano-objects in all cases, with spherical polymersomes of $\sim$50 nm in diameter being observed for targeted DP$_{P(NB-MEG)}$ = 120, and a mixture of spherical and tubular polymersomes being formed for DP$_{P(NB-MEG)}$ = 240.

A simple comparison of the relative FRET efficiency of the various samples could be made using the ratio of the maximum intensities of the donor (ACM) and acceptor (RhB) peaks in the fluorescence spectra, with higher values representing a greater FRET efficiency. The calculated ratios for the pure and mixed nano-object samples when excited at $\lambda_{ex.}$ = 360 nm are shown in Figure 4C. In general, the FRET ratio was higher for the mixed samples than for the pure ACM-functionalized nano-objects. A more evident increase in this ratio can be noticed when comparing the M$_{a-2h}$ and M$_d$ samples for the polymerizations targeting DP$_{P(NB-MEG)}$ = 240 than for those targeting DP$_{P(NB-MEG)}$ = 120. Since the molar concentration of each fluorophore remained constant in both series, these findings indicate a higher relative FRET efficiency for the mixed samples with **P(NB-MEG)** DP of 240, implying closer contact between the fluorophores in this case and as a consequence a great extent of membrane blending.

To further evaluate differences in FRET behavior of triblock copolymer nano-objects with DP$_{P(NB-MEG)}$ = 120 and 240, fluorescence lifetimes (FL) corresponding to the ACM fluorophore for pure and mixed samples were measured. Figure 4D-I,D-II show fluorescence lifetime decay curves for the ACM-functionalized particles alone (ACM$_n$) and mixed with RhB-functionalized particles either during (ACM$_n$+RhB$_n$ M$_d$) or after polymerization (ACM$_n$+RhB$_n$ M$_{a-2h}$; n = 120 and 240, respectively). In particular, no change in FL could be observed when comparing the decay curves for the ACM$_{120}$+RhB$_{120}$ M$_{a-2h}$ and ACM$_{120}$+RhB$_{120}$ M$_d$ mixed samples, consistent with our observation that no fusion events occur at this **P(NB-MEG)** DP. In contrast, a faster FL decay
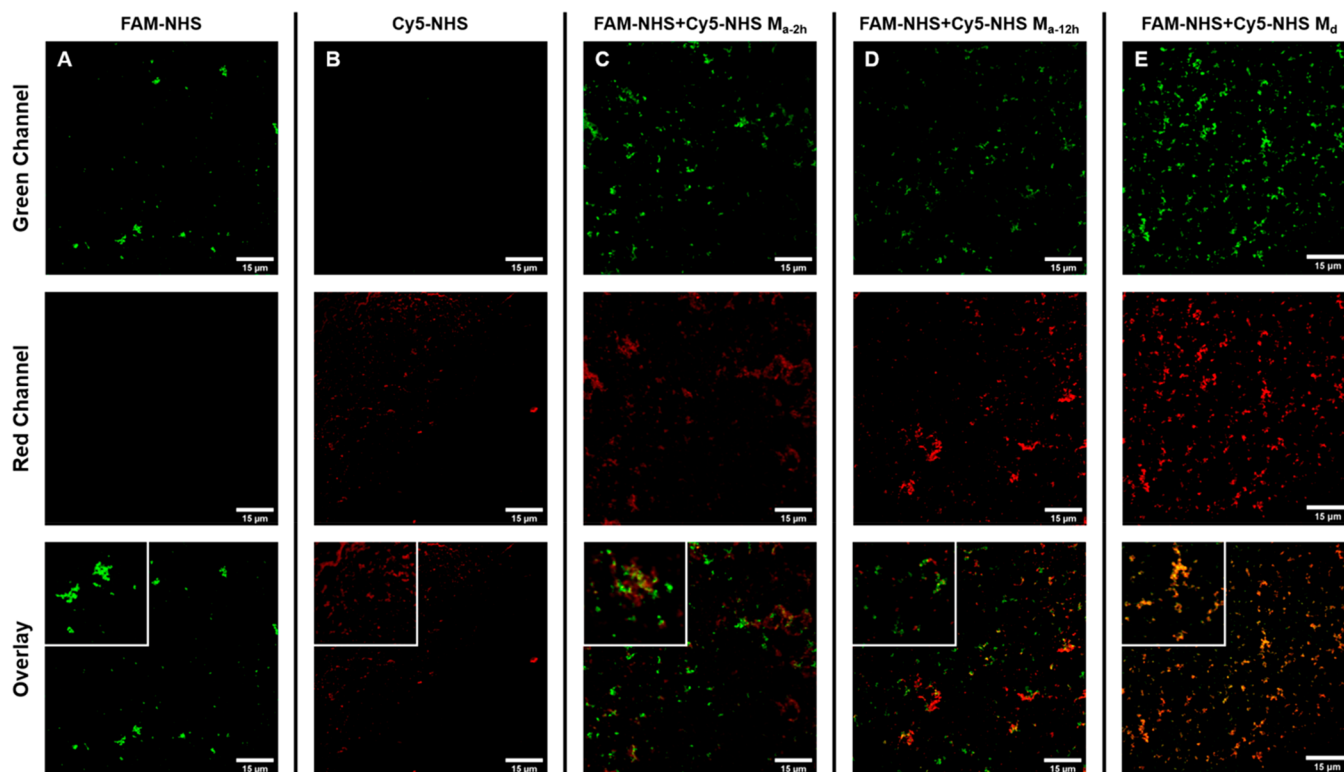
Figure 5. Representative confocal microscopy images for pure FAM-NHS-loaded (green; A) and Cy5-NHS-loaded (red; B) $P(NB-PEG)_{11}$-b-$P(NB-MEG)_{240}$ diblock copolymer nano-objects, and resulting FAM-NHS+Cy5-NHS $M_{a-2h/12h}$ (C and D) and FAM-NHS+Cy5-NHS M_d (E) samples for investigation of inner aqueous lumen mixing of polymersomes during tubesome development. In all cases, the scale bars represent 15 μm and the size of the insets is 20 $\mu m \times 20 \mu m$.

was observed for the samples that were mixed during polymerization targeting $DP_{P(NB-MEG)} = 240$, where extensive membrane fusion was expected to occur. The observed FL differences revealed a change in the surrounding microenvironment of ACM molecules due to the close presence of RhB moieties and subsequent occurrence of energy transfer phenomena.[69] To further emphasize this difference in FRET behavior, the decay curves were fit using both $\tau_{Av,I}$ and $\tau_{Av,A}$ methods to determine intensity-average and amplitude-average FL values, respectively, for each sample (Table S16). A comparison of average fluorescence lifetimes for the ACM_n+RhB_n M_{a-2h} and ACM_n+RhB_n M_d mixed samples relative to that of the pure ACM_n nano-objects, taken as a percentage difference, is shown in Figure 4E. Here, a more dramatic difference can be observed between the $ACM_{120}+RhB_{120}$ and $ACM_{240}+RhB_{240}$ samples that were mixed during polymerization. Owing to the fact that FRET efficiency depends on the distance separating the donor and acceptor species, it can be concluded that a notably higher proportion of these fluorophores are in close contact for nano-objects with $DP_{P(NB-MEG)} = 240$ compared to the ones with $DP_{P(NB-MEG)} = 120$, further supporting the concept of polymerization-induced polymersome fusion.

Contrary to the above FRET findings, comparison of average FL values for samples mixed after polymerization either for 2h or 24h showed the opposite trend for $ACM_{120}+RhB_{120}$ and $ACM_{240}+RhB_{240}$ samples, with a decrease in FL observed between the $ACM_{120}+RhB_{120}$ M_{a-2h} and $ACM_{120}+RhB_{120}$ M_{a-24h} samples but no noticeable difference between FL decay profiles for the $DP_{P(NB-MEG)} = 240$ samples (Figure S51). This suggests a limited occurrence of unimer

exchange for the $DP_{P(NB-MEG)} = 120$ samples and essentially no unimer exchange for the kinetically "frozen" $ACM_{240}+RhB_{240}$ nanostructures over prolonged periods of time.

In addition to the membrane fusion studies, it was of paramount importance to investigate whether the interior aqueous lumens of individual spherical polymersomes were also able to mix to form a single aqueous compartment during fusion processes. To this extent, two water-soluble fluorescent dyes with distinctly different fluorescent profiles chosen to avoid FRET (i.e., FAM-NHS (green-emitting dye), and Cy5-NHS (red-emitting dye)) were encapsulated within the lumens of $P(NB-PEG)_{11}$-b-$P(NB-MEG)_n$ diblock copolymer nano-objects.[71] Since fusion events were shown to be driven by polymerization, it was projected that lumen and hence dye mixing would only occur when samples were mixed in early stages of ROMPISA prior to tubesome development, whereas exchange of cargoes for samples mixed after completion of the polymerization could only occur via diffusion of the dyes between discrete nano-objects. Similar to the methodology followed in FRET studies, the two dyes were directly encapsulated into separate formulations via aqueous ROMPI-SA targeting DP of $P(NB-MEG) = 240$ (above fusion threshold), and FAM-NHS- and Cy5-NHS-loaded samples were mixed either after 1 min of polymerization time (ca. ~ 50% monomer conversion) (FAM-NHS+Cy5-NHS M_d) or after polymerization for a period of 2h (FAM-NHS+Cy5-NHS M_{a-2h}) and 12h (FAM-NHS+Cy5-NHS M_{a-12h}). The developed pure and mixed FAM-NHS- and Cy5-NHS-loaded samples were purified by dialysis against DI water (pH 7.0) for removal of unencapsulated dye and were subsequently imaged using TEM and confocal microscopy.

In all cases, the morphologies formed from this series of dye-loaded nano-objects agreed well with previously described di- or triblock copolymer systems targeting the same core-block DP with a mixture of long tubesomes and a small population of spherical non-fused polymersomes being observed by dry-state TEM imaging (Figure S43). Moreover, confocal microscopy imaging of the purified FAM-NHS- and Cy5-NHS-loaded **P(NB-PEG)$_{11}$-*b*-P(NB-MEG)$_{240}$** nano-objects confirmed the successful encapsulation of either dye within discrete compartmentalized nanostructures, detected using either a green or a red channel, respectively (Figures 5A,B). Importantly, comparison of the green and red channel overlay for acquired images of FAM-NHS+Cy5-NHS M$_{a-2h/12h}$ and FAM-NHS+Cy5-NHS M$_d$ samples revealed that extensive fusion between polymersome lumens was achieved in the latter case, where near complete color overlap was clearly observed in the merged image, suggesting the co-localization of the two fluorescent dyes in the same aqueous microenvironment (Figure 5E). In contrast, merged confocal microscopy images for dye-loaded samples mixed after polymerization showed no observable color overlap after 2h and 12h of mixing, implying that no fusion had occurred nor had the two dyes become co-localized via diffusion processes. These experiments serve as further validation of our original hypothesis of polymerization-promoted fusion (Figure 5C,D).

DISCUSSION

On the basis of our original experimental design, it was possible to promote fusion of spherical polymersomes prepared via aqueous ROMPISA and induce morphological transitions toward the formation of higher-order tubular polymersomes by altering the chemistry of the corona-forming stabilizer block. In particular, it was observed that inelastic collisions and fusion phenomena between cationic **P(NB-amine)$_{11}$-*b*-P(NB-MEG)$_n$** diblock copolymer polymersomes were effectively prohibited for a wide range of targeted core block DPs, preventing the morphological evolution of the prepared vesicular nanostructures. On the contrary, the energetic barrier that needed to be surpassed to allow for one-dimensional collisions between individual polymersomes was readily reduced when a non-ionic **P(NB-PEG)**-based macroinitiator was utilized for preparation of nano-objects with minimal surface charge, driving the occurrence of extensive fusion events during polymerization and *in situ* development of cylindrical tubesomes (Figures 1 and 2). The preparation of tubular polymersomes has been previously reported via manipulation of spherical precursors by changes in osmotic pressure, pH, or supramolecular complexation,[55,56,72,73] by purification of mixed morphologies containing tubesomes and other nanostructures,[74] through assembly of liquid-crystalline block copolymers,[75,76] or through self-assembly in solvent mixtures containing high concentrations of PEG.[77,78] In these examples, no control over the length or sample composition was demonstrated. In contrast, tubesomes of controllable length were reproducibly achieved in our system under standard aqueous ROMPISA conditions in the absence of external manipulation, originating instead from polymerization-induced polymersome fusion.

Comparison of the TEM image analysis data for the various samples shown above revealed that the average maximum dimension (S_{ave}) values of **P(NB-amine)**-based formulations remained nearly constant with increasing DP of core-forming **P(NB-MEG)** block, suggesting limited fusion in this case. In

stark contrast, the calculated S_{ave} values and the corresponding non-spherical fraction for diblock copolymer nano-objects bearing **P(NB-PEG)$_{11}$** and **P(NB-amine)$_{11}$+NaCl** coronae were found to gradually increase with increasing targeted core block DP, whereas C_{ave} values followed the opposite trend, providing initial evidence for our hypothesis of polymersome fusion. Importantly, in the case of the **P(NB-PEG)$_{11}$-*b*-P(NB-MEG)$_{260}$** nano-objects, an S_{ave} of approximately 450 nm and a non-spherical fraction close to 1.0 evidently showed the development of a near uniform population of long tubular polymersomes with unique physicochemical characteristics owing to their shape anisotropy.[53–57] Determination of the fraction of non-spherical nano-objects from TEM image analysis for each series also indicated that the onset of polymersome fusion in the case of **P(NB-amine)**-based nano-objects prepared in the presence of NaCl occurred at a higher core-block DP compared to the **P(NB-PEG)**-based series (Figures 6A,B, S15–S16, S23–S24, and S36–S37).
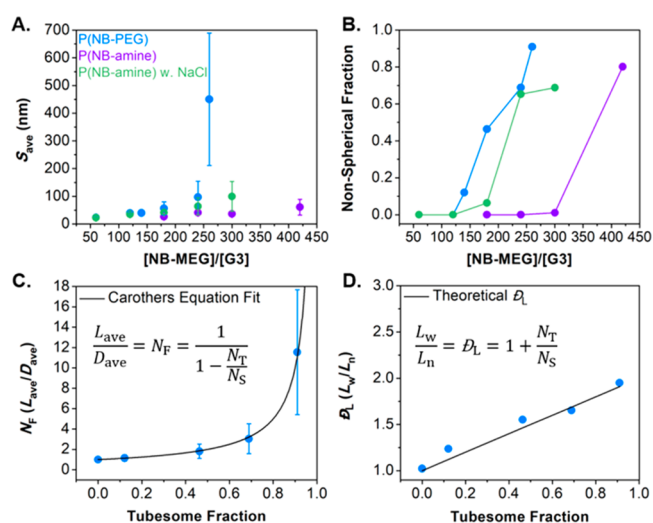

Figure 6. Summary of image analysis data as calculated from acquired dry-state TEM images. (A) Evolution of S_{ave} values with increasing targeted DP$_{P(NB-MEG)}$ for **P(NB-PEG)$_{11}$-*b*-P(NB-MEG)$_n$** (blue circles) and **P(NB-amine)$_{11}$-*b*-P(NB-MEG)$_n$** diblock copolymer nano-objects developed via aqueous ROMPISA in the absence (purple circles) or presence (green circles) of NaCl. (B) Sample composition, expressed as the fraction of non-spherical nano-objects, as a function of targeted DP$_{P(NB-MEG)}$ for the same samples. For **P(NB-PEG)$_{11}$-*b*-P(NB-MEG)$_n$** diblock copolymer nano-objects: C) Evolution of N_F (= L_{ave}/D_{ave}) values, the average number of fused particles per tubesome, as a function of the fraction of cylindrical tubesomes in the sample. The black line represents a "step-growth-like" fit of the data using a modified version of Carothers equation (R^2 = 0.997). (D) Evolution of tubesome length dispersity, $Đ_L$, (= L_w/L_n) values with increasing cylindrical tubesome fraction. The black line represents theoretically expected $Đ_L$ values calculated from a "step-growth-like" fit of the data using a modified version of Carothers equation (R^2 = 0.981).

In order to gain further insight into the fusion process of **P(NB-PEG)$_{11}$-*b*-P(NB-MEG)$_n$** diblock copolymer nano-objects, a data fitting process was developed based on the dry-state TEM image analysis data relating the particle shape distribution to the average tubesome length. First, the average number of spherical polymersomes that had fused per tubesome (N_F) was calculated for each diblock copolymer composition by dividing the average particle length (L_{ave}) (or

D_{ave} for samples where only spherical polymersomes were observed) by a fixed particle diameter value. This diameter value was chosen to be the calculated D_{ave} of the **P(NB-PEG)$_{11}$-b-P(NB-MEG)$_{140}$** sample at the onset of polymersome fusion (i.e., $D_{ave} \approx 39$ nm) with the assumption that the average width of fused tubesomes remained relatively constant once fusion had begun. This was further validated by performing manual particle counting measurements for determination of average tubesome width values for each sample, which did not notably vary across the series. The determined N_F values were then correlated to the fraction of cylindrical tubesomes over spherical particles ($F_C = N_T/N_S$, where N_T and N_S represent the number of tubular and spherical polymersomes, respectively; Figure 6C).

Interestingly, it was found that the most accurate fit of the obtained image analysis data resulted from a modified version of Carothers equations for step-growth polymerization that correlate the average degree of polymerization (X_n) and polymer dispersity ($Đ_M$) with monomer conversion (p) (i.e., $X_n = 1/(1 - p)$ and $Đ_M = 1 + p$, respectively).[79] In complete analogy to step-growth polymerization, single spherical polymersomes were considered to be "monomeric building blocks" for the fusion-driven synthesis of tubesome "macromolecules", composed of two or more fused particles. In addition, N_F was considered as the "degree of polymersome fusion" and the ratio N_T/N_S was considered as the "monomer conversion". Finally, the tubesome length dispersity values ($Đ_L = 1 + F_C$) were calculated by dividing the measured weight-average length values (L_w) by the corresponding number-average length values (L_n) for every **P(NB-PEG)$_{11}$-b-P(NB-MEG)$_n$** nano-object composition and were found to agree well with theoretically expected values obtained from a modified Carothers equation for polymer dispersity determination (Figure 6D).[79] On the basis of these findings, it is evident that polymersome fusion mirrors a step-growth-like motif. Thus, the proposed polymersome fusion methodology can be utilized as a straightforward guide for targeting a specific nano-object composition (i.e., ratio between tubular and spherical polymersomes) in this system via tuning of the targeted core block DP of the nanoassemblies.

Apart from investigation of polymersome fusion via TEM imaging of end-point ROMPISA reactions targeting a certain DP of **P(NB-MEG)**, alternative characterization techniques were also utilized to *in situ* monitor and definitively confirm the occurrence of polymerization-induced fusion events. First, ROMPISA kinetic monitoring via ^{1}H-NMR spectroscopy was performed for synthesis of **P(NB-amine)$_{11}$-b-P(NB-MEG)$_{300}$** and **P(NB-PEG)$_{11}$-b-P(NB-MEG)$_{260}$** diblock copolymers with effectively the same molecular weight and dispersity values, eliminating the speculation that observed differences in the fusion behavior could potentially arise from discrepancies in polymerization kinetics. In both cases, aqueous ROMPISA processes followed pseudo-first-order kinetics with similar polymerization rate constants and quantitative monomer conversions achieved after 30 min of polymerization. Additionally, monitoring of changes in average nano-object diameter and % transmittance values upon polymerization progression by DLS and *in situ* turbidimetric analysis, respectively, allowed for direct evaluation of fusion behavior and tubesome formation in the **P(NB-PEG)$_{11}$**-based system (Figure 3).

Following detailed assessment of the polymersome fusion procedure, the polymerization time ($t = 2.55$ min) and as a

consequence the critical DP of **P(NB-MEG)** (DP ≈ 185) at which the onset of fusion occurred were able to be accurately determined. These values were subsequently correlated to intensity-average D_h values measured from DLS kinetic analysis, revealing that nano-objects of approximately 68 nm in size were present in solution at the onset of polymersome fusion prior to evolution of tubesomes. Similar to the methodology followed for analysis of dry-state TEM images for **P(NB-PEG)$_{11}$-b-P(NB-MEG)$_n$** diblock copolymer nano-objects, all intensity-average D_h values measured for intermediate time points and core-forming block DPs during kinetic monitoring were divided by this fixed D_h value in order to determine the extent of fusion and conversion of spherical polymersomes by DLS analysis. Finally, DLS conversion values were appropriately normalized so that the fraction of cylindrical tubesomes (F_C) (i.e., conversion) at the final time point was equal to the one calculated for the same end-point **P(NB-PEG)$_{11}$-b-P(NB-MEG)$_{260}$** formulation from TEM image analysis, since DLS operates under the assumption that incident light is scattered by hard spheres, often underestimating the actual average dimension values for nanoparticles of cylindrical shape (Figure 7A).

To further investigate differences between polymerization and fusion kinetics, the rates corresponding to each process were initially plotted as semilogarithmic relationships assuming pseudo-first-order kinetics. Interestingly, it was found that this
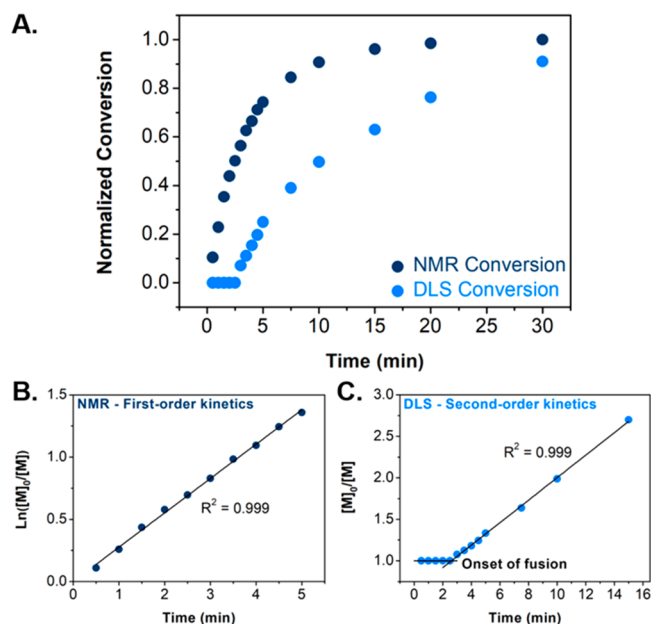

Figure 7. Comparison between polymerization and fusion kinetics for synthesis of **P(NB-PEG)$_{11}$-b-P(NB-MEG)$_{260}$** tubesomes. (A) Monomer conversion after particle nucleation (dark blue circles) and spherical polymersome conversion (light blue circles) vs polymerization time kinetic plots for synthesis of **P(NB-PEG)$_{11}$-b-P(NB-MEG)$_{260}$** diblock copolymer tubesomes via aqueous ROMPISA, as determined by ^{1}H-NMR spectroscopy and DLS analysis, respectively. (B) Ln($[M]_0/[M]$) vs polymerization time kinetic plot, as determined by ^{1}H-NMR spectroscopy, showing that the ROMPISA polymerization followed pseudo-first-order kinetics ($R^2 = 0.999$). (C) $[M]_0/[M]$ vs polymerization time kinetic plot, as determined by DLS analysis, showing that the polymersome fusion process followed second-order kinetics with the onset of fusion observed at *ca.* 2.55 min ($R^2 = 0.999$).
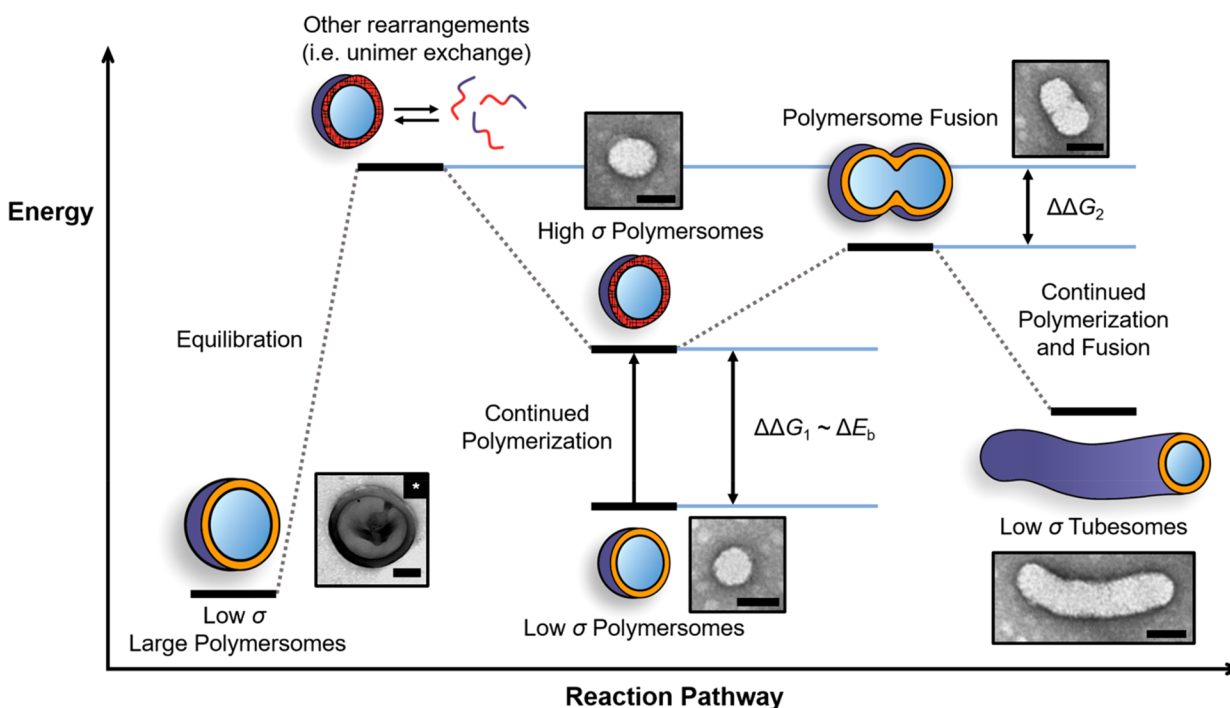
Figure 8. Proposed assembly pathway for polymerization-induced fusion of spherical polymersomes and *in situ* membrane tension-driven morphological evolution toward kinetically favored tubesomes for $P(NB-PEG)_{11}$-*b*-$P(NB-MEG)_n$ diblock copolymer nano-objects. Other rearrangements (i.e., unimer exchange) and equilibration procedures promote the formation of thermodynamically favored nanostructures. The scale bars for the dry-state TEM image insets represent 50 nm, except for the image marked with an asterisk (*) where the scale bar represents 100 nm.

first-order fitting was only precisely applicable in the case of ROMPISA kinetics, whereas a poor data fit was obtained in the case of polymersome fusion kinetics (Figure 7B). Indeed, the rate of polymerization-induced polymersome fusion was best fit using a second-order kinetic equation (Figure 7C). As shown in Figure 7C, the kinetic plot of $[M]_0/[M]$ vs polymerization time using size values obtained from DLS analysis was separated into two regimes. For the first regime from 0 to 2.55 min, spherical polymersomes of growing size were developed with no evident fusion events occurring, whereas for the second regime, a dramatic acceleration in rate was observed after 2.55 min that was attributed to the onset of polymerization-induced polymersome fusion resulting in a progressively larger population of tubular vesicles with increasing conversion.

We believe that the evidently faster polymerization kinetics as compared to fusion kinetics is of paramount importance for the development of kinetically trapped morphologies with slow chain mobility during aqueous ROMPISA in the case of $P(NB-PEG)_{11}$-based formulations. In particular, out-of-equilibrium evolution of tubular polymersomes as the kinetically favorable product driven by 1D inelastic collisions between spherical polymersome building blocks with high membrane tension was solely observed during ROMPISA, whereas other self-assembly methodologies (e.g., solvent-switch or plasticization by EVE molecules) that allow for slow rearrangement and equilibration of polymer chains resulted in the formation of different thermodynamically favorable morphologies, such as large spherical polymersomes or donut-shaped particles (Figure S41).

Confirmation of our originally proposed rationale that fusion events were only promoted during ROMPISA and were more pronounced at higher core-block DPs was achieved by a series of experiments involving either the direct attachment or encapsulation of fluorescent molecules within the membrane or inner aqueous lumen domains of polymersomes, respectively, that were used as markers for fusion monitoring. In the first case, ACM- and RhB-functionalized triblock copolymer nano-objects were prepared containing either fluorophore between the corona- and core-forming blocks with targeted $DP_{P(NB-MEG)}$ below or above the fusion threshold. This approach allowed for monitoring of fusion events of polymersome membranes occurring during ROMPISA process. For samples mixed during ROMPISA, a distinctly faster FL decay was observed for ACM-containing nano-objects when targeting core block DP = 240 as compared to the samples with $DP_{P(NB-MEG)} = 120$ owing to occurrence of extensive fusion events and hence presence of the two fluorophores in close proximity in the former case. FL decay profiles for samples mixed after polymerization for 2h revealed no significant energy transfer and fusion phenomena in either case, whereas measurements after mixing for an extended period of time (24h) showed that minimum unimer exchange took place for the $DP_{P(NB-MEG)} = 240$ sample (Figures 4 and S51).

Moreover, following the previously described concept of sample mixing during polymerization prior to the onset of fusion or after completion of polymerization and fusion procedures, the polymerization-induced mixing of polymersome inner lumens was also verified by confocal microscopy imaging via the observed co-localization of the utilized water-soluble FAM-NHS and Cy5-NHS fluorescent dyes within the same aqueous microenvironment for the $P(NB-PEG)_{11}$-*b*-$P(NB-MEG)_{240}$ diblock copolymer nano-object samples mixed during polymerization. On the contrary, limited cargo exchange and hence minimum lumen fusion and membrane permeability was observed for samples mixed after ROMPISA,

as FAM-NHS and Cy5-NHS dyes were found to be located in distinctly disparate domains (Figure 5). In addition, the evidently rapid monomer consumption is supposed to also limit plasticization of the nano-object hydrophobic domains by the core-forming monomer in the early ROMPISA stages, minimizing unimer and cargo exchange between particles.

Finally, dry-state TEM imaging and analysis of the acquired images for both **P(NB-amine)**- and **P(NB-PEG)**-based samples of different compositions aged for a period of 4 weeks were carried out for determination of S_{ave} values and non-spherical nano-object fractions (Figures S19 and S42). In both cases, average particle dimensions and non-spherical fractions of the aged samples were found not to vary significantly compared to the originally developed samples, clearly showing their high stability under storage conditions in aqueous media as well as the prevention of equilibration phenomena or additional fusion events after polymerization over prolonged periods of time due to the lack of a driving force.

Based on these observations, our proposed assembly pathway for polymerization-induced polymersome fusion and *in situ* step-growth-like formation of tubesomes in the case of **P(NB-PEG)$_{11}$**-*b*-**P(NB-MEG)$_{n}$** diblock copolymer nano-objects is schematically illustrated in Figure 8. We rationalize the fusion phenomenon in terms of polymersome membrane energy. Small spherical polymersomes of low σ arise in early stages of polymerization. The rapid increase of block copolymer chain length and concurrent increase in copolymer hydrophobicity as ROMPISA progresses leads to a buildup of polymersome membrane tension ($\Delta\Delta G_1$, high σ polymersomes). This tension cannot be alleviated by unimer exchange or other dissipative pathways, evidenced by the long-term stability of the tubular nanostructures, likely due to the glassy nature of the membranes (T_g of **P(NB-MEG)$_{180}$** homopolymer = 118.2 °C, Figure S6) and the poor water solubility of the constituent polymer chains. Such a pathway would allow access to the equilibrium morphology, which was shown to consist of large spherical polymersomes prepared via a solvent-switch methodology. Instead, membrane tension is alleviated by fusion between two (or more) polymersomes. Upon continued polymerization and fusion events, tubesomes form preferentially to reduce the overall surface area of the system. Ideally, an energetic minimum would be reached for spherical polymersomes with membranes under no tension. However, the bending rigidity of the constituent polymer chains reduces the amount of membrane curvature that is allowed, and a fine balance is struck between membrane tension and bending rigidity to generate highly anisotropic, low σ tubesomes as kinetic products that persist beyond the completion of the polymerization.

CONCLUSIONS

In summary, we present a novel two-step strategy to induce spontaneous fusion of small spherical polymersomes and concurrent morphological evolution toward tubular block copolymer nanostructures via aqueous ROMP-mediated PISA without the requirement of further external processing. Variations in corona chemistry (i.e., ionic vs non-ionic coronae) and core-forming block length/hydrophobicity in combination with the unique characteristics of ROMPISA, such as the exceedingly fast polymerization kinetics and the synthesis of rod-like poly(norbornene)-based block copolymers with rigid backbone and high T_g values, were found to be

the main factors in dictating the occurrence of "controlled" fusion phenomena and the development of kinetically trapped tubesomes. Such features are typically absent in the vast majority of cases for extensively studied RAFT-mediated PISA processes, explaining why such an intriguing assembly behavior has not been observed thus far. Importantly, preparation of a progressively larger population of anisotropic tubesomes was supposed to occur through internal buildup of polymersome membrane tension with continued polymerization and was observed to accurately follow a step-growth-like polymersome fusion model. Overall, we expect that our unprecedented polymerization-induced polymersome fusion methodology will lead the way toward exploring a wide range of nature-mimicking processes via the application of block copolymer nano-objects of distinct characteristics in on-demand catalysis, artificial organelle development, and drug/protein delivery among others.

■ ASSOCIATED CONTENT

Ⓢ Supporting Information

The Supporting Information is available free of charge at https://pubs.acs.org/doi/10.1021/jacs.9b10152.

> Materials and characterization techniques, synthetic procedures, supplementary NMR and SEC analysis data of di- and triblock copolymers, additional DLS, SLS, FL and turbidimetric analysis data, and representative dry-state and cryo-TEM images of nano-objects, full characterization of **P(NB-amine)$_{11}$**-*b*-**P(NB-MEG)$_{n}$** diblock copolymer nano-objects developed via ROMPISA in the presence of NaCl (PDF)

■ AUTHOR INFORMATION

Corresponding Authors
*j.c.foster@bham.ac.uk
*r.oreilly@bham.ac.uk
ORCID Ⓞ
Jeffrey C. Foster: 0000-0002-9097-8680
Rachel K. O'Reilly: 0000-0002-1043-7172
Notes
The authors declare no competing financial interest.

■ REFERENCES

(1) Lucy, J. A. The Fusion of Biological Membranes. *Nature* **1970**, 227, 815−817.
(2) Wickner, W.; Schekman, R. Membrane fusion. *Nat. Struct. Mol. Biol.* **2008**, 15, 658−664.
(3) Chernomordik, L. V.; Kozlov, M. M. Mechanics of membrane fusion. *Nat. Struct. Mol. Biol.* **2008**, 15, 675−683.

(4) Alberts, B.; Johnson, A.; Lewis, J.; Raff, M.; Roberts, K.; Walter, P. *Mol. Biol. Cell*, 4th ed.; Garland Science: New York, 2002.

(5) Mashburn-Warren, L. M.; Whiteley, M. Special delivery: vesicle trafficking in prokaryotes. *Mol. Microbiol.* 2006, 61, 839−846.

(6) Rothman, J. E.; Wieland, F. T. Protein Sorting by Transport Vesicles. *Science* 1996, 272, 227−234.

(7) Fasshauer, D.; Sutton, R. B.; Brunger, A. T.; Jahn, R. Conserved structural features of the synaptic fusion complex: SNARE proteins reclassified as Q- and R-SNAREs. *Proc. Natl. Acad. Sci. U. S. A.* 1998, 95, 15781−15786.

(8) Chen, Y. A.; Scheller, R. H. SNARE-mediated membrane fusion. *Nat. Rev. Mol. Cell Biol.* 2001, 2, 98−106.

(9) Jahn, R.; Grubmüller, H. Membrane fusion. *Curr. Opin. Cell Biol.* 2002, 14, 488−495.

(10) Kozlov, M. M.; Chernomordik, L. V. Membrane tension and membrane fusion. *Curr. Opin. Struct. Biol.* 2015, 33, 61−67.

(11) Shillcock, J. C.; Lipowsky, R. Tension-induced fusion of bilayer membranes and vesicles. *Nat. Mater.* 2005, 4, 225−228.

(12) Gao, L.; Lipowsky, R.; Shillcock, J. Tension-induced vesicle fusion: pathways and pore dynamics. *Soft Matter* 2008, 4, 1208−1214.

(13) Lasic, D. D. On the thermodynamic stability of liposomes. *J. Colloid Interface Sci.* 1990, 140, 302−304.

(14) Lipowsky, R. Spontaneous tubulation of membranes and vesicles reveals membrane tension generated by spontaneous curvature. *Faraday Discuss.* 2013, 161, 305−331.

(15) Venturoli, M.; Maddalena Sperotto, M.; Kranenburg, M.; Smit, B. Mesoscopic models of biological membranes. *Phys. Rep.* 2006, 437, 1−54.

(16) Müller, M.; Katsov, K.; Schick, M. Biological and synthetic membranes: What can be learned from a coarse-grained description? *Phys. Rep.* 2006, 434, 113−176.

(17) Gao, L.; Shillcock, J.; Lipowsky, R. Improved dissipative particle dynamics simulations of lipid bilayers. *J. Chem. Phys.* 2007, 126, 015101.

(18) Lin, Y.-L.; Chang, H.-Y.; Sheng, Y.-J.; Tsao, H.-K. The fusion mechanism of small polymersomes formed by rod−coil diblock copolymers. *Soft Matter* 2014, 10, 1500−1511.

(19) Nieva, J. L.; Goni, F. M.; Alonso, A. Liposome fusion catalytically induced by phospholipase C. *Biochemistry* 1989, 28, 7364−7367.

(20) Rørvig-Lund, A.; Bahadori, A.; Semsey, S.; Bendix, P. M.; Oddershede, L. B. Vesicle Fusion Triggered by Optically Heated Gold Nanoparticles. *Nano Lett.* 2015, 15, 4183−4188.

(21) Ries, O.; Löffler, P. M. G.; Rabe, A.; Malavan, J. J.; Vogel, S. Efficient liposome fusion mediated by lipid−nucleic acid conjugates. *Org. Biomol. Chem.* 2017, 15, 8936−8945.

(22) Malinin, V. S.; Frederik, P.; Lentz, B. R. Osmotic and Curvature Stress Affect PEG-Induced Fusion of Lipid Vesicles but Not Mixing of Their Lipids. *Biophys. J.* 2002, 82, 2090−2100.

(23) Dimova, R.; Riske, K. A.; Aranda, S.; Bezlyepkina, N.; Knorr, R. L.; Lipowsky, R. Giant vesicles in electric fields. *Soft Matter* 2007, 3, 817−827.

(24) Henderson, I. M.; Paxton, W. F. Salt, Shake, Fuse—Giant Hybrid Polymer/Lipid Vesicles through Mechanically Activated Fusion. *Angew. Chem., Int. Ed.* 2014, 53, 3372−3376.

(25) Kliesch, T.-T.; Dietz, J.; Turco, L.; Halder, P.; Polo, E.; Tarantola, M.; Jahn, R.; Janshoff, A. Membrane tension increases fusion efficiency of model membranes in the presence of SNAREs. *Sci. Rep.* 2017, 7, 12070.

(26) Su, W.; Luo, Y.; Yan, Q.; Wu, S.; Han, K.; Zhang, Q.; Gu, Y.; Li, Y. Photoinduced Fusion of Micro-Vesicles Self-Assembled from Azobenzene-Containing Amphiphilic Diblock Copolymers. *Macromol. Rapid Commun.* 2007, 28, 1251−1256.

(27) Chang, H.-Y.; Sheng, Y.-J.; Tsao, H.-K. Structural and mechanical characteristics of polymersomes. *Soft Matter* 2014, 10, 6373−6381.

(28) Rodríguez-Hernández, J.; Chécot, F.; Gnanou, Y.; Lecommandoux, S. Toward 'smart' nano-objects by self-assembly of block copolymers in solution. *Prog. Polym. Sci.* 2005, 30, 691−724.

(29) Mai, Y.; Eisenberg, A. Self-assembly of block copolymers. *Chem. Soc. Rev.* 2012, 41, 5969−5985.

(30) Palivan, C. G.; Goers, R.; Najer, A.; Zhang, X.; Car, A.; Meier, W. Bioinspired polymer vesicles and membranes for biological and medical applications. *Chem. Soc. Rev.* 2016, 45, 377−411.

(31) Blanazs, A.; Madsen, J.; Battaglia, G.; Ryan, A. J.; Armes, S. P. Mechanistic Insights for Block Copolymer Morphologies: How Do Worms Form Vesicles? *J. Am. Chem. Soc.* 2011, 133, 16581−16587.

(32) Warren, N. J.; Armes, S. P. Polymerization-Induced Self-Assembly of Block Copolymer Nano-objects via RAFT Aqueous Dispersion Polymerization. *J. Am. Chem. Soc.* 2014, 136, 10174−10185.

(33) Warren, N. J.; Mykhaylyk, O. O.; Ryan, A. J.; Williams, M.; Doussineau, T.; Dugourd, P.; Antoine, R.; Portale, G.; Armes, S. P. Testing the Vesicular Morphology to Destruction: Birth and Death of Diblock Copolymer Vesicles Prepared via Polymerization-Induced Self-Assembly. *J. Am. Chem. Soc.* 2015, 137, 1929−1937.

(34) Zhang, W.-J.; Hong, C.-Y.; Pan, C.-Y. Artificially Smart Vesicles with Superior Structural Stability: Fabrication, Characterizations, and Transmembrane Traffic. *ACS Appl. Mater. Interfaces* 2017, 9, 15086−15095.

(35) Blackman, L. D.; Varlas, S.; Arno, M. C.; Houston, Z. H.; Fletcher, N. L.; Thurecht, K. J.; Hasan, M.; Gibson, M. I.; O'Reilly, R. K. Confinement of Therapeutic Enzymes in Selectively Permeable Polymer Vesicles by Polymerization-Induced Self-Assembly (PISA) Reduces Antibody Binding and Proteolytic Susceptibility. *ACS Cent. Sci.* 2018, 4, 718−723.

(36) Varlas, S.; Blackman, L. D.; Findlay, H. E.; Reading, E.; Booth, P. J.; Gibson, M. I.; O'Reilly, R. K. Photoinitiated Polymerization-Induced Self-Assembly in the Presence of Surfactants Enables Membrane Protein Incorporation into Vesicles. *Macromolecules* 2018, 51, 6190−6201.

(37) Varlas, S.; Foster, J. C.; Georgiou, P. G.; Keogh, R.; Husband, J. T.; Williams, D. S.; O'Reilly, R. K. Tuning the membrane permeability of polymersome nanoreactors developed by aqueous emulsion polymerization-induced self-assembly. *Nanoscale* 2019, 11, 12643−12654.

(38) Chen, M.; Li, J.-W.; Zhang, W.-J.; Hong, C.-Y.; Pan, C.-Y. pH- and Reductant-Responsive Polymeric Vesicles with Robust Membrane-Cross-Linked Structures: In Situ Cross-Linking in Polymerization-Induced Self-Assembly. *Macromolecules* 2019, 52, 1140−1149.

(39) Charleux, B.; Delaittre, G.; Rieger, J.; D'Agosto, F. Polymerization-Induced Self-Assembly: From Soluble Macromolecules to Block Copolymer Nano-Objects in One Step. *Macromolecules* 2012, 45, 6753−6765.

(40) Tan, J.; Sun, H.; Yu, M.; Sumerlin, B. S.; Zhang, L. Photo-PISA: Shedding Light on Polymerization-Induced Self-Assembly. *ACS Macro Lett.* 2015, 4, 1249−1253.

(41) Canning, S. L.; Smith, G. N.; Armes, S. P. A Critical Appraisal of RAFT-Mediated Polymerization-Induced Self-Assembly. *Macromolecules* 2016, 49, 1985−2001.

(42) Yeow, J.; Boyer, C. Photoinitiated Polymerization-Induced Self-Assembly (Photo-PISA): New Insights and Opportunities. *Adv. Sci.* 2017, 4, 1700137.

(43) Penfold, N. J. W.; Yeow, J.; Boyer, C.; Armes, S. P. Emerging Trends in Polymerization-Induced Self-Assembly. *ACS Macro Lett.* 2019, 8, 1029−1054.

(44) Sun, J.-T.; Hong, C.-Y.; Pan, C.-Y. Formation of the block copolymer aggregates via polymerization-induced self-assembly and reorganization. *Soft Matter* 2012, 8, 7753−7767.

(45) Foster, J. C.; Varlas, S.; Couturaud, B.; Coe, Z.; O'Reilly, R. K. Getting into Shape: Reflections on a New Generation of Cylindrical Nanostructures' Self-Assembly Using Polymer Building Blocks. *J. Am. Chem. Soc.* 2019, 141, 2742−2753.

(46) Foster, J. C.; Varlas, S.; Couturaud, B.; Jones, J. R.; Keogh, R.; Mathers, R. T.; O'Reilly, R. K. Predicting Monomers for Use in Polymerization-Induced Self-Assembly. *Angew. Chem., Int. Ed.* 2018, 57, 15733−15737.

(47) Varlas, S.; Foster, J. C.; Arkinstall, L. A.; Jones, J. R.; Keogh, R.; Mathers, R. T.; O'Reilly, R. K. Predicting Monomers for Use in Aqueous Ring-Opening Metathesis Polymerization-Induced Self-Assembly. *ACS Macro Lett.* **2019**, *8*, 466−472.

(48) Blackman, L. D.; Doncom, K. E. B.; Gibson, M. I.; O'Reilly, R. K. Comparison of photo- and thermally initiated polymerization-induced self-assembly: a lack of end group fidelity drives the formation of higher order morphologies. *Polym. Chem.* **2017**, *8*, 2860−2871.

(49) Tan, J.; Huang, C.; Liu, D.; Li, X.; He, J.; Xu, Q.; Zhang, L. Polymerization-Induced Self-Assembly of Homopolymer and Diblock Copolymer: A Facile Approach for Preparing Polymer Nano-Objects with Higher-Order Morphologies. *ACS Macro Lett.* **2017**, *6*, 298−303.

(50) Huang, C.; Tan, J.; Xu, Q.; He, J.; Li, X.; Liu, D.; Zhang, L. Adding a solvophilic comonomer to the polymerization-induced self-assembly of block copolymer and homopolymer: a cooperative strategy for preparing large compound vesicles. *RSC Adv.* **2017**, *7*, 46069−46081.

(51) Varlas, S.; Georgiou, P. G.; Bilalis, P.; Jones, J. R.; Hadjichristidis, N.; O'Reilly, R. K. Poly(sarcosine)-Based Nano-Objects with Multi-Protease Resistance by Aqueous Photoinitiated Polymerization-Induced Self-Assembly (Photo-PISA). *Biomacromolecules* **2018**, *19*, 4453−4462.

(52) Foster, J. C.; Varlas, S.; Blackman, L. D.; Arkinstall, L. A.; O'Reilly, R. K. Ring-Opening Metathesis Polymerization in Aqueous Media Using a Macroinitiator Approach. *Angew. Chem., Int. Ed.* **2018**, *57*, 10672−10676.

(53) Yang, X.; Grailer, J. J.; Rowland, I. J.; Javadi, A.; Hurley, S. A.; Steeber, D. A.; Gong, S. Multifunctional SPIO/DOX-loaded wormlike polymer vesicles for cancer therapy and MR imaging. *Biomaterials* **2010**, *31*, 9065−9073.

(54) Lai, M.-H.; Jeong, J. H.; DeVolder, R. J.; Brockman, C.; Schroeder, C.; Kong, H. Ellipsoidal Polyaspartamide Polymersomes with Enhanced Cell-Targeting Ability. *Adv. Funct. Mater.* **2012**, *22*, 3239−3246.

(55) van Oers, M. C. M.; Rutjes, F. P. J. T.; van Hest, J. C. M. Tubular Polymersomes: A Cross-Linker-Induced Shape Transformation. *J. Am. Chem. Soc.* **2013**, *135*, 16308−16311.

(56) Toebes, B. J.; Abdelmohsen, L. K. E. A.; Wilson, D. A. Enzyme-driven biodegradable nanomotor based on tubular-shaped polymeric vesicles. *Polym. Chem.* **2018**, *9*, 3190−3194.

(57) Wong, C. K.; Stenzel, M. H.; Thordarson, P. Non-spherical polymersomes: formation and characterization. *Chem. Soc. Rev.* **2019**, *48*, 4019−4035.

(58) Wright, D. B.; Touve, M. A.; Thompson, M. P.; Gianneschi, N. C. Aqueous-Phase Ring-Opening Metathesis Polymerization-Induced Self-Assembly. *ACS Macro Lett.* **2018**, *7*, 401−405.

(59) Torres-Rocha, O. L.; Wu, X.; Zhu, C.; Crudden, C. M.; Cunningham, M. F. Polymerization-Induced Self-Assembly (PISA) of 1,5-Cyclooctadiene Using Ring Opening Metathesis Polymerization. *Macromol. Rapid Commun.* **2019**, *40*, 1800326.

(60) Tomasek, J.; Schatz, J. Olefin metathesis in aqueous media. *Green Chem.* **2013**, *15*, 2317−2338.

(61) Sabatino, V.; Ward, T. R. Aqueous olefin metathesis: recent developments and applications. *Beilstein J. Org. Chem.* **2019**, *15*, 445−468.

(62) Varlas, S.; Foster, J. C.; O'Reilly, R. K. Ring-opening metathesis polymerization-induced self-assembly (ROMPISA). *Chem. Commun.* **2019**, *55*, 9066−9071.

(63) Lynn, D. M.; Mohr, B.; Grubbs, R. H. Living Ring-Opening Metathesis Polymerization in Water. *J. Am. Chem. Soc.* **1998**, *120*, 1627−1628.

(64) Semsarilar, M.; Ladmiral, V.; Blanazs, A.; Armes, S. P. Cationic Polyelectrolyte-Stabilized Nanoparticles via RAFT Aqueous Dispersion Polymerization. *Langmuir* **2013**, *29*, 7416−7424.

(65) Patterson, J. P.; Robin, M. P.; Chassenieux, C.; Colombani, O.; O'Reilly, R. K. The analysis of solution self-assembled polymeric nanomaterials. *Chem. Soc. Rev.* **2014**, *43*, 2412−2425.

(66) Novak, B. M.; Grubbs, R. H. Catalytic organometallic chemistry in water: the aqueous ring-opening metathesis polymerization of 7-oxanorbornene derivatives. *J. Am. Chem. Soc.* **1988**, *110*, 7542−7543.

(67) Hillmyer, M. A.; Lepetit, C.; McGrath, D. V.; Novak, B. M.; Grubbs, R. H. Aqueous ring-opening metathesis polymerization of carboximide-functionalized 7-oxanorbornenes. *Macromolecules* **1992**, *25*, 3345−3350.

(68) Wyatt, P. J. Measurement of Special Nanoparticle Structures by Light Scattering. *Anal. Chem.* **2014**, *86*, 7171−7183.

(69) Clegg, R. M. Förster resonance energy transfer—FRET what is it, why do it, and how it's done. In *Laboratory Techniques in Biochemistry and Molecular Biology*; Elsevier: Amsterdam, 2009; Vol. 33, pp 1−57.

(70) Xie, Y.; Husband, J. T.; Torrent-Sucarrat, M.; Yang, H.; Liu, W.; O'Reilly, R. K. Rational design of substituted maleimide dyes with tunable fluorescence and solvafluorochromism. *Chem. Commun.* **2018**, *54*, 3339−3342.

(71) Grumelard, J.; Taubert, A.; Meier, W. Soft nanotubes from amphiphilic ABA triblock macromonomers. *Chem. Commun.* **2004**, 1462−1463.

(72) Abdelmohsen, L. K. E. A.; Williams, D. S.; Pille, J.; Ozel, S. G.; Rikken, R. S. M.; Wilson, D. A.; van Hest, J. C. M. Formation of Well-Defined, Functional Nanotubes via Osmotically Induced Shape Transformation of Biodegradable Polymersomes. *J. Am. Chem. Soc.* **2016**, *138*, 9353−9356.

(73) Chen, X.; Liu, L.; Huo, M.; Zeng, M.; Peng, L.; Feng, A.; Wang, X.; Yuan, J. Direct Synthesis of Polymer Nanotubes by Aqueous Dispersion Polymerization of a Cyclodextrin/Styrene Complex. *Angew. Chem., Int. Ed.* **2017**, *56*, 16541−16545.

(74) Robertson, J. D.; Yealland, G.; Avila-Olias, M.; Chierico, L.; Bandmann, O.; Renshaw, S. A.; Battaglia, G. pH-Sensitive Tubular Polymersomes: Formation and Applications in Cellular Delivery. *ACS Nano* **2014**, *8*, 4650−4661.

(75) Wong, C. K.; Mason, A. F.; Stenzel, M. H.; Thordarson, P. Formation of non-spherical polymersomes driven by hydrophobic directional aromatic perylene interactions. *Nat. Commun.* **2017**, *8*, 1240.

(76) Mondal, T.; Sakurai, T.; Yoneda, S.; Seki, S.; Ghosh, S. Semiconducting Nanotubes by Intrachain Folding Following Macroscopic Assembly of a Naphthalene−Diimide (NDI) Appended Polyurethane. *Macromolecules* **2015**, *48*, 879−888.

(77) Gao, C.; Zhou, H.; Qu, Y.; Wang, W.; Khan, H.; Zhang, W. In Situ Synthesis of Block Copolymer Nanoassemblies via Polymerization-Induced Self-Assembly in Poly(ethylene glycol). *Macromolecules* **2016**, *49*, 3789−3798.

(78) Ding, Z.; Ding, M.; Gao, C.; Boyer, C.; Zhang, W. In Situ Synthesis of Coil−Coil Diblock Copolymer Nanotubes and Tubular Ag/Polymer Nanocomposites by RAFT Dispersion Polymerization in Poly(ethylene glycol). *Macromolecules* **2017**, *50*, 7593−7602.

(79) Flory, P. J. Fundamental Principles of Condensation Polymerization. *Chem. Rev.* **1946**, *39*, 137−197.